IEEE Access
Multidisciplinary ⋮ Rapid Review ⋮ Open Access Journal

Received 6 April 2024, accepted 22 April 2024, date of publication 25 April 2024, date of current version 3 May 2024.

Digital Object Identifier 10.1109/ACCESS.2024.3393858

RESEARCH ARTICLE

A PCA-SVM Regression Model for LEO Space Debris Orbit Prediction in an Optical Space-Based Space Surveillance Network

SARA HAMIDIAN AND AMIR REZA KOSARI
Faculty of New Sciences and Technologies, School of Aerospace Engineering, University of Tehran, Tehran 1439957131, Iran
Corresponding author: Amir Reza Kosari (kosari_a@ut.ac.ir)

ABSTRACT The primary objective of this study is to investigate the efficacy of Support Vector Machine (SVM) regression method to enhance the accuracy of Low Earth Orbit (LEO) space debris orbit prediction using the historical data. Principal Component Analysis (PCA) is employed to efficiently reduce the dimensionality of dataset's feature space and hence optimize the model's performance. This investigation is motivated by the limitations of conventional orbit prediction methods, which often rely on dynamic models with unknown coefficients of perturbation forces and other relevant characteristics of space debris, leading to errors during the prediction process. On the other hand, while the Collision Avoidance Maneuver (CAM) strategy remains crucial for mitigating the threat posed by such debris, precise knowledge of debris coordinates is essential for effective CAM implementation. However, traditional ground-based optical equipment encounters challenges in observing fast-moving debris within the dynamic LEO environment, including atmospheric interference and limited Field of View (FOV). To address these limitations, the secondary objective of this study involves exploring the potential of an in-orbit optical space surveillance network as a promising solution. The system utilizes optical sensors distributed across multiple spacecraft within the Above the Horizon (ATH) constellation, specifically designed to continuously monitor the most densely populated altitude band in LEO. Simulations under different conditions demonstrate that the proposed scheme successfully complements ground-based equipment and dynamic models for debris tracking, thereby improving orbit prediction accuracy. The results of simulations under different conditions demonstrate that proposed scheme successfully complements ground-based equipment and dynamic models for debris tracking, and improving orbit prediction accuracy.

INDEX TERMS LEO space debris, tracking, orbit prediction, optical space surveillance network, support vector machine, principal component analysis.

I. INTRODUCTION

Space debris is a pressing concern, posing significant risks to operational spacecraft, and long-term sustainability of space activities. To effectively address this issue, two critical aspects play a vital role to ensure the safety of operations: space debris tracking and reliable and accurate orbit prediction. Space debris tracking helps mitigate collision risks, enhance situational awareness, and guide the development of effective debris management strategies. Ground-based space debris tracking systems rely on a combination of technologies, including radars, lasers, and optical telescopes, each offering unique capabilities crucial for comprehensive space situational awareness. Radars, as demonstrated by [1], excel in distance detection with millimeter precision. Optical telescopes, as highlighted in [2], [3], [4], [5], [6], [7], and [8], provide exceptional angular precision of 0.01 arcseconds, despite being susceptible to weather conditions. Laser

The associate editor coordinating the review of this manuscript and approving it for publication was Rosario Pecora.

systems, as discussed by [4] and [8], contribute precise ranging measurements. These laser-ranging systems provide accurate distance measurements, further enhancing the overall tracking capabilities of ground-based systems. The drastic increase of LEO (Low Earth Orbit) Resident Space Objects (RSOs), particularly orbital debris, necessitates the development of sophisticated space surveillance systems. To meet this demand, optical space-based surveillance networks have emerged as a highly promising complement to traditional radar-based systems [1], [9]. These optical networks offer numerous advantages, including high-resolution capabilities for tracking smaller objects, cost-effectiveness, all-weather operability, real-time and continuous observation capabilities, and potential for scientific research. Integrating optical Space-Based Space Surveillance Networks (SBSSNs) with existing ground-based equipment presents a comprehensive, and powerful approach to ensure the safety, efficiency, and sustainability of operations in increasingly crowded LEO environment. The SBSSN complements ground-based systems by offering continuous, unobstructed monitoring from space. Integrating data from ground-based and SBSSN sources enhances space situational awareness, critical for collision avoidance as emphasized by [8]. On the other hand, accurately predicting debris trajectories is crucial for comprehensively understanding their dynamics and effectively mitigating potential hazards. Such predictions play a crucial role in planning collision avoidance maneuvers and optimizing satellite operations. Moreover, precise orbit propagation is vital to identify potential conjunctions, and assessing collision probabilities between operational satellites and debris fragments, enabling timely warnings and maneuver recommendations to ensure the safety and continuity of space missions. Understanding the spatial distribution and density of LEO debris is essential to design efficient spacecraft disposal and end-of-life measures, as accurate predictions allow for determining optimal disposal altitudes and angles, resulting in reduced long-term orbital debris accumulation, and a decreased likelihood of future collisions. It is crucial to note that the effect of LEO debris extends to broader concerns, as collisions involving large objects can trigger cascading effects, generating more debris fragments and exacerbating the space debris problem. This phenomenon, which is often referred to as Kesler Syndrome, highlights the potential for a catastrophic cascade of collisions in LEO resulting from the proliferation of space debris. Critical debris sources can be identified by leveraging accurate orbit propagation, facilitating targeted remediation efforts and debris removal missions to address the issue effectively.

Recent studies on this topic have explored various aspects of tracking and predicting LEO debris trajectories. These studies cover constellation design strategies, precise initial orbit determination and estimation methodologies, and state-of-the-art orbit prediction algorithms.

Within constellation design, coverage is classified into two primary categories: traditional Below the Horizon (BTH) and ATH (Above the Horizon) problems. BTH problems focus on achieving Earth coverage using circular [10], [11], [12] or elliptical orbits [13], [14], [15], while ATH problems are about observing targets against the space background. Within ATH, there are two subcategories: Single Altitude Band Shell (SABS) and Dual Altitude Bands Shell (DABS) problems. DABS primarily focuses on strategically designing satellite constellations that can comprehensively cover targets within both lower and upper altitude bands. Despite its importance, there has been limited research conducted on the DABS subcategory. Rider [16], [17] was a pioneer in developing DABS polar constellation for low to medium altitudes, with platforms positioned within dual altitudes bands or above the upper altitude band. Biria and Marchand [18] introduced an analytical method for DABS ATH constellations, enabling platforms below the lower altitude band. However, their approach was constrained by practical limitations resulting from simplifying assumptions. Takano and Marchand [19] considered more complex sensor profiles and addressed previous limitations, providing a numerical solution to the DABS coverage problem.

Lei et al. [20] conducted a comprehensive study on initial orbit determination for LEO RSOs, studying the effect of different sensors' angle observation geometries, noise levels, and the number of observations. Qu et al. [21] developed an analytical solution for initial orbit determination using bi-static radar with two observations at different times, evaluating its efficacy for tracking space objects under various observation geometries.

Camet et al. [22] presented a comprehensive review of various estimation algorithms and proposed a solution to the RSO tracking problem. Their method utilizes simulated optical telescope observations and employs a Bayesian filter-based approach.

In the context of enhancing orbit prediction accuracy, numerous studies have made great contributions. Levit and Marshall [23] introduced an advanced numerical propagator based on the Two-Line Element (TLE) catalog, leading to significant improvement in orbit prediction accuracy. Chen et al. [24], employed an innovative error analysis approach by using historical data to reveal inherent periodic attributes in prediction errors. Goh et al. [25] proposed an innovative strategy focused on orbit parameter preprocessing, and effectively mitigating errors during orbit propagation. Simultaneously, Sang et al. [26] introduced a dual-step TLE-based methodology aimed at significantly improving prediction accuracy. Perez and Bevilacqua [27] employed neural network techniques to address errors induced by atmospheric density, offering a novel perspective on error correction. In the domain of orbit determination, Sharma and Cutrel [28] introduced a learning-based framework based on distribution regression principles. Peng and Bai [29], [30] presented innovative orbit prediction methods based on ML (Machine Learning) approaches, leading to notable enhancement in prediction accuracy. Expanding on this foundation,

Peng and Bai [31] conducted a thorough evaluation of three contemporary ML approaches to enhance orbit prediction accuracy. Jung et al. [32] introduced a recurrent neural network model designed for predicting reentry trajectories of uncontrolled space objects. Zhai et al. [33] investigated a ML approach, particularly focusing on the XGBoost algorithm to improve the orbit prediction accuracy. Takahashi et al. [34] explored Gaussian process regression using GPS (Global Positioning System) data to reconstruct continuous data from sparse positioning data, providing a valuable perspective on data-driven orbit prediction. Li et al. [35] implemented two learning methods, gradient boosting decision tree and convolutional neural networks to improve TLE-based orbit prediction accuracy. Salleh et at. [36] proposed a deep learning technique specifically aimed at improving TLE-based orbit prediction accuracy. Xu et al. [37] introduced an orbit prediction model based on ML approach to effectively correct the error value of orbit prediction for Internet of Thing (IoT) applications.

This research explores the potential of utilizing an in-orbit optical space surveillance network to effectively track LEO space debris. To enhance the accuracy of space debris orbit prediction, a novel model is introduced, making use of the SVM (Support Vector Machine) regression method and historical data in a simulated environment. Furthermore, PCA (Principal Component Analysis) is employed to efficiently reduce the dimensionality of the dataset's feature space, and optimizing the model's overall performance. This combination of advanced techniques offers a promising approach to address the growing challenge of LEO space debris tracking and prediction. When comparing the output of our proposed machine learning model for orbit propagation of LEO space debris with that of classical orbital dynamic models implemented in General Mission Analysis Tool (GMAT) [57], Semi-analytical Tool for End of Life Analysis (STELA) [58], etc., notable distinctions may become apparent. The computer simulations conducted by the authors indicate a significant increase in prediction errors over time with classical methods. These errors, mainly caused by uncertain coefficients in mathematical modeling of perturbation forces and also space debris characteristics, quickly amplify to the extent that future orbital trajectories become uncertain. This, in turn, may severely compromise the accuracy of orbit prediction for space debris. In contrast, our proposed machine learning-based compensatory approach may provide a promising remedy. By effectively mitigating predicted state errors, our method enables the attainment of more accurate orbital states with minimized error margins. This capability holds critical importance for the scheduling and execution of CAM in operational satellite systems.

The remaining part of the paper is structured as follows: Section II introduces the simulation framework and assesses the feasibility of the proposed optical SBSSN. Section III presents the details about the ML approach, and introduces the PCA as a powerful tool for the dimensionality reduction of feature space. Section IV discusses the design of the learning process and the selection of learning and target variables. Section V presents the analysis of the simulation results, and finally, section VI summarizes the conclusions.

II. SIMULATION ENVIRONMENT

This section provides a comprehensive description of the simulated environment designed for the proposed scheme as depicted in FIGURE 1.

The framework introduces a PCA-SVM regression machine learning approach to enhance the accuracy of LEO debris orbit prediction. The approach relies on optical measurements obtained from a dedicated DABS ATH [16] constellation, specifically designed to provide continuous multi-fold coverage in the most populated altitude bands of LEO.

A. TRUTH DYNAMIC MODEL

The simulated truth dynamic model proposed in this study aims to comprehensively address the primary factors contributing to prediction errors in LEO orbit. The model incorporates the Newtonian gravitational force and accommodates the Earth oblate gravitational field through zonal and tesseral harmonic coefficients of degree and order 70×70 [52]. Moreover, third-body perturbations induced by the Sun and the Moon are considered. To approximate atmospheric conditions, the NRLMSISE-00 [56] model is employed, which considers mean solar and geomagnetic activities. Truth dynamic model is implemented in the MATLAB programming environment.

B. MEASUREMENT MODEL

This research focuses on the development of an optical space-based space surveillance network intended for tracking space debris within the most densely populated altitude band of LEO. This network utilizes a dedicated DABS ATH constellation. The constellation is configured to provide continuous multi-fold coverage over highly populated altitude range in LEO, which spans approximately 700 km to 1000 km above the Earth's surface. This specific altitude band is commonly called the ''LEO debris cloud''. In order to confirm that the majority of LEO debris falls within the range of 700-1000 km, data from total number of 4461 TLEs were used to illustrate the frequency of these debris a function of semi-major axis. The data is available on the CelesTrack website[1] and is categorized into four major groups of LEO debris: Fengyun 1C [53], Iridium 33 [54], Cosmos 2251 [54], and Cosmos 1408 [55]. The results are shown in FIGURE 2 and align well with published LEO debris density [38]. Notably, the corresponding date for FIGURE 2 is July 2023, enhancing the temporal relevance of the analysis. In this study, a satellite deployment strategy based on the Rider technique [16] is selected to design a space-based surveillance network for continuous DABS ATH viewing of the specified target altitude band from platforms in polar orbits.

[1] https://celestrak.org/NORAD/elements

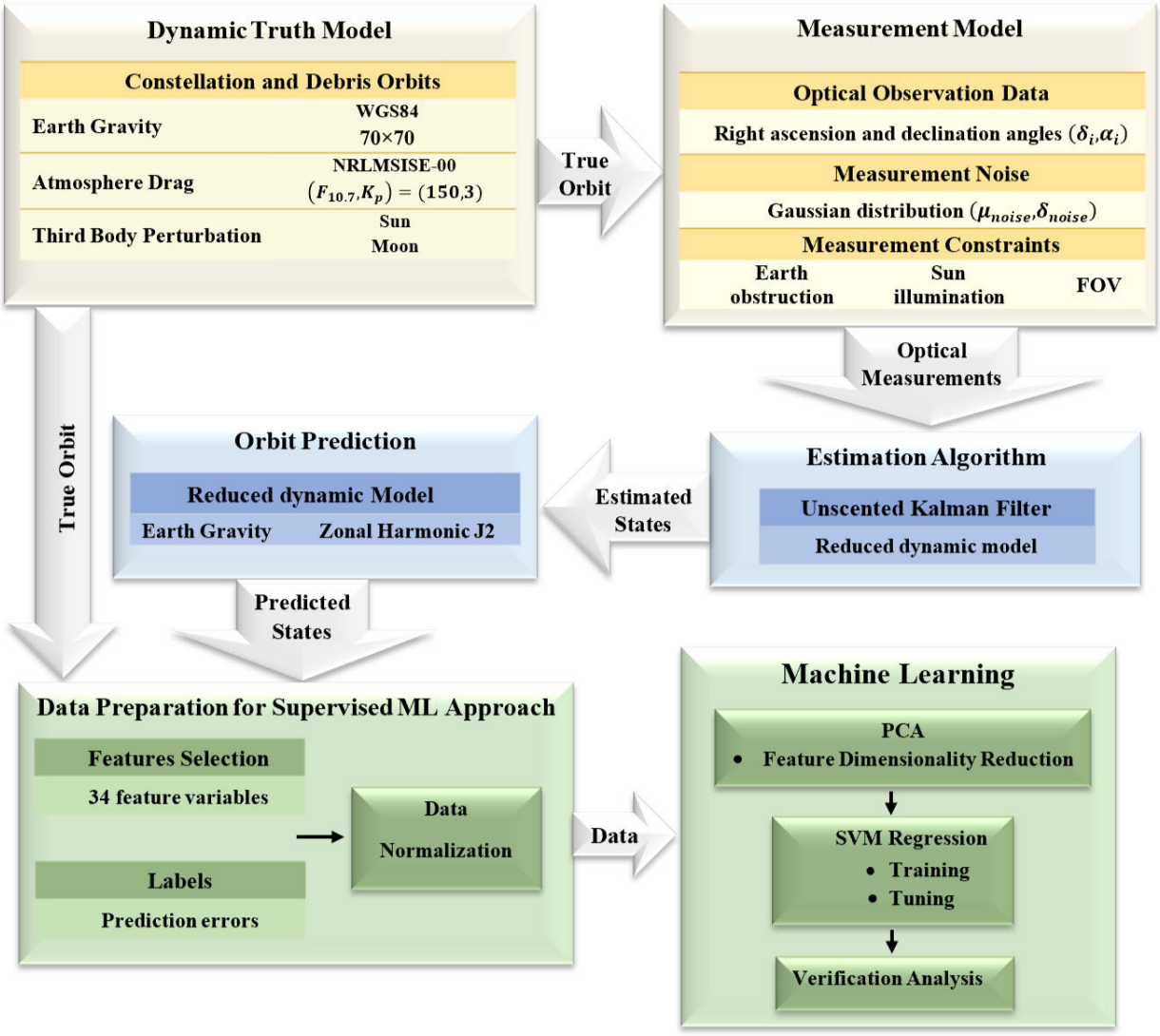

FIGURE 1. Framework of the proposed PCA-SVM regression ML approach to enhance LEO debris orbit prediction accuracy.

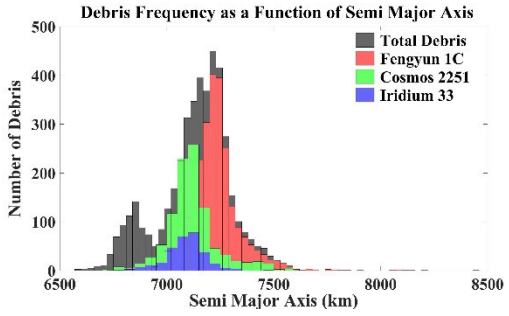

FIGURE 2. Debris frequency as a function of semi-major axis based on 4461 TLEs; from Fengyun 1C, Iridium 33, Cosmos 2251 and Cosmos 1408.

This approach, utilizes a method based on spherical geometry and Street-of-Coverage (SOC) theory, as described in the works of Adams and Rider [39] and Luders [40], to derive formulas for the coverage multiplicity of the DABS ATH constellation. The coverage multiplicity refers to the number of satellites that can simultaneously observe a specific ATH region bounded within the lower and upper altitude shells. The technique is a deterministic approach to derive the total number of platforms, sensor elevation Field of View (FOV), and sensor maximum range requirements for design of space-based surveillance systems in polar orbits that provide continuous multiple global or polar cap ATH viewing. These requirements are determined as a function of surveillance platform altitude, the minimum and maximum space object altitudes of interest, and the multiplicity of desired ATH coverage.

The needed number of orbital planes, the required number of satellites per orbital plane, and geocentric latitude coverage restrictions are all related to coverage multiplicity. Thus, the number of sensors needed for full DABS global coverage is

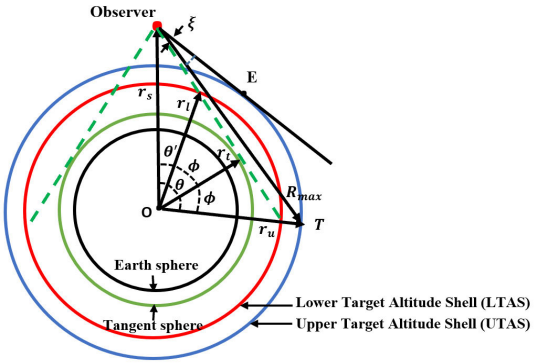

FIGURE 3. Rider SOC approach in DABS ATH coverage geometry.

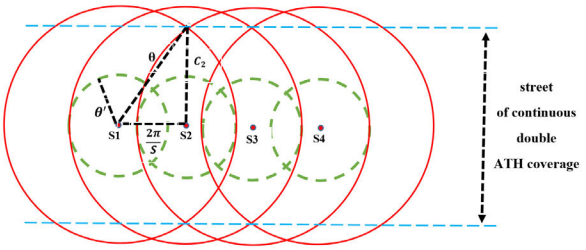

FIGURE 4. Double nadir-hole-fill projection on the lower target shell.

computed given a specified coverage multiplicity and minimum latitude.

Therefore, it is beneficial to provide an overview of the SOC technique.

FIGURE 3 illustrates the geometry employed in the Rider study, considering a single-satellite DABS ATH coverage scenario, specifically when the platform is located above then the target upper altitude band. It is essential to note that in the Rider method, platforms can be positioned either within or above the target dual-altitude-band. However, this article particularly focuses on the latter option. This choice is motivated by two key reasons. Firstly, the target altitude band is already overcrowded with LEO debris, and the objective is to avoid further crowding by deploying platforms in this altitude band. Secondly, as the platform altitude increases, the impact of atmospheric drag perturbation and consequently orbital decay becomes less significant. As depicted in FIGURE 3, The tangent sphere around the Earth at radial distance r_t is determined by the lowest allowable sensor Line-of-Sight (LOS) penetration of the atmosphere without interfering with its normal functionality. The outer and lower surfaces of the target shell, at corresponding radial distances r_u and r_l, are defined by the maximum and minimum altitudes, respectively, at which continuous viewing of targets is assured with the specified multiplicity of coverage. r_t, r_l and r_u are considered as 100 km, 700 km and 1000 km, respectively.

According to FIGURE 3, achieving above-the-tangent-altitude viewing of targets within the specified altitude shell, as observed from a single platform, is guaranteed when the targets are located within a shell defined by the central angle 2ϕ and undergo a 360 deg rotation out of the paper's plane about the r_s axis (where r_s represents the radial direction to the sensor platform). The outer boundary of the shell's coverage is determined by the central angle θ, measured from the platform's nadir point. The "nadir-hole", representing the region directly below and invisible to a sensor platform regardless of the size of the sensor-to-target range, is defined by the central angle θ', also measured from the platform's nadir. The maximum sensor-to-target range, denoted as R_{max}, occurs when the target is positioned at location T and the required platform's FOV, denoted as ξ, is determined at point E, where the platform's LOS grazes the outer part of the target shell. By solving for planar triangles illustrated in FIGURE 3, when r_s exceeds both r_l and r_u, the following relations can be established:

$$\phi = \cos^{-1}\left(\frac{r_t}{r_l}\right). \tag{1}$$

$$\theta = \cos^{-1}\left(\frac{r_t}{r_s}\right) + \phi. \tag{2}$$

$$\theta' = \cos^{-1}\left(\frac{r_t}{r_s}\right) - \phi. \tag{3}$$

$$R_{max} = \left(r_s^2 + r_u^2 - 2r_s r_u cos\theta\right)^{1/2}. \tag{4}$$

$$\xi = \sin^{-1}\left(\frac{r_u}{r_s}\right) - \sin^{-1}\left(\frac{r_t}{r_s}\right), \tag{5}$$

these equations illustrate that by specifying r_t, r_l, r_u, and r_s, the geometry of single-platform DABS ATH, along with the maximum platform-to-target range requirement and the platform's FOV, can be determined. Techniques for achieving single nadir hole fill for satellites in the same orbital plane can be found in Rider's earlier work [51]. The validation process will benefit from the following general condition on θ:

$$\frac{2\pi}{s} \leq \theta \leq \frac{\pi}{2} ors > 4, \tag{6}$$

where s represents the minimum number of platforms in each orbital plane. The Eq. (6) must always hold to achieve any level of nadir hole fill. Otherwise, the determination of the minimum number of required platforms can be derived from Rider's dual-altitude band ATH coverage paper [16] for continuity, in which he chooses double nadir hole fill. As illustrated in FIGURE 4, This objective is achieved by satisfying the condition:

$$\theta \geq \frac{2\pi}{s} + \theta'. \tag{7}$$

Applying (1), (2), and (3) to (7) yields the following condition:

$$s \geq \frac{\pi}{\cos^{-1}\left(\frac{r_t}{r_l}\right)} \geq \frac{\pi}{\phi}. \tag{8}$$

This indicates that the minimum number of platforms symmetrically distributed in a single orbital plane, providing

double nadir hole fill for all nadir holes, is solely a function of r_t and r_l.

Similar to BTH coverage [17], the half street width of continuous j-fold coverage associated with one orbital plane composed of s platforms is given by:

$$C_j = \cos^{-1}\left[\frac{cos\theta}{cos\left(\frac{j\pi}{s}\right)}\right]. \tag{9}$$

As illustrated in FIGURE 4, the half street width of continuous double coverage for a single orbital plane is:

$$C_2 = \cos^{-1}\left[\frac{cos\theta}{cos\left(\frac{2\pi}{s}\right)}\right]. \tag{10}$$

The Rider method places particular emphasis on the double coverage property within each orbital plane, as parts of its multiple coverage scheme. This approach is rooted in a study conducted by W.S. Adams [16], which illustrates that platform constellations synthesized from orbital planes utilizing even multiples of coverage are more efficient than those employing odd multiples of coverage in delivering ATH coverage for the lower target shell.

Rider also establishes a conservative general relation between the half street width of 2-fold coverage (C_2), the required number of orbital planes (p), and the minimum latitude (L) at which $2k$-fold continuous coverage is achieved.

$$p = \left[\frac{k(\pi/2)}{\sin^{-1}(\sin C_2/\cos L)}\right]. \tag{11}$$

The outer brackets indicate that the quantity within should be rounded up to the next higher integer if it is not already an integer.

Eq. (11) yields the number of polar orbital planes needed to ensure 2k-fold continuous ATH coverage of the target shell at a geocentric latitude of L or higher (each orbital plane provides double coverage when s satisfies (8)). The total required number of platforms, denoted as T, is then calculated as:

$$T = sp = s\left[\frac{k(\pi/2)}{\sin^{-1}(\sin C_2/\cos L)}\right]. \tag{12}$$

It is now evident that Rider explored a deterministic approach to determine the key design parameters, including the total number of required platforms, the required platform's FOV, and the maximum platform-to-target range within a defined space volume specified by lower and upper altitude bands that encompass potential targets of interest.

The selected tangent altitude representing the deepest atmospheric penetration of the platform-to-target LOS is 100 km, corresponding to $r_t = 6478.137$ km. The lower and upper altitudes of the target shell are 700 and 1000 km, resulting in r_l and r_u at 7078.137 and 7378.137 km, respectively. To optimize the efficiency of ATH constellations, orbital planes with symmetrically distributed platforms that provide a street-of-double-coverage are employed. The number of platforms per orbital plane, denotes as s and obtained from (8), is determined to be 8, the minimum required value. This determination is based on substituting the selected values of r_t and r_l in (8). These selections allow for the illustration of the relationship between R_{max}, ξ, and T as a function of ATH platform altitude, as shown in FIGURE 5. The total number of platforms illustrated in FIGURE 5 is based on the requirement of a minimum 4-fold continuous ATH target coverage above 45° latitude (k = 2 and L = 45°). This requirement is met using polar orbital planes symmetrically distributed at the same altitude in a circular orbit within each orbital plane. Above the Earth's equator, continuous ATH coverage is 2-fold. The level of continuous ATH coverage steadily increases with latitude, transitioning from 4-fold coverage at 45° latitude to 3p-fold coverage over the pole, with p representing the number of orbital planes in the constellation. The data shown in FIGURE 5 illustrate the j = 2 solutions under specific values of r_t, r_l, r_u, s, k, and L which are 6478 km, 7078 km,7378 km, 8 and 45° respectively. A noticeable discontinuity occurs in both platform's FOV and maximum platform-to-target range as the platform's position shifts from within the target shell (ranging from700 to 1000 km) to above it. This variation is attributed to the different geometries inherent in these two scenarios, and it is thoroughly explained in Rider's research [16]. FIGURE 5 clearly illustrates that in both scenarios, as the platform altitude increases, the required platform's FOV decreases, while the necessary maximum platform-to-target range increases. However, these changes follow distinct patterns.

The study's design point is established at a platform altitude of h_s= 1300 km, with 24 platforms distributed across 3 orbital planes ($p = 3$), each containing 8 platforms. The required platform's FOV is $\xi = 16.39°$, and the necessary maximum platform-to-target range is R_{max}= 7100 km. This configuration ensures continuous double street-of-coverage above the Earth's equator, which then extends to four-fold coverage at latitude of 45 deg. This increase in coverage multiplicity persists as the latitude approaches 90 deg.

One of the primary reasons for adopting the Multiple Point-of-View (MPOV) optical observation scheme in this paper is the challenge of achieving accurate orbit determination with a single POV space-based optical platform. Orbit determination of a target using a single space-based optical observer is hindered by short observation arcs, mainly due to the limited FOV of the optical platform and the high relative angular velocities between the platforms and the target. Various proposed solutions to address this challenge include estimation algorithms such as genetic algorithms [41], batch methods [42], and sequential estimators [43], [44], [45]. However, an efficient initial orbit determination method that ensures final convergence remains a challenging issue with all the presented solutions, which is not well solved yet in this case.

It is important to highlight that among different MPOV observation schemes for cataloging the LEO space debris, the

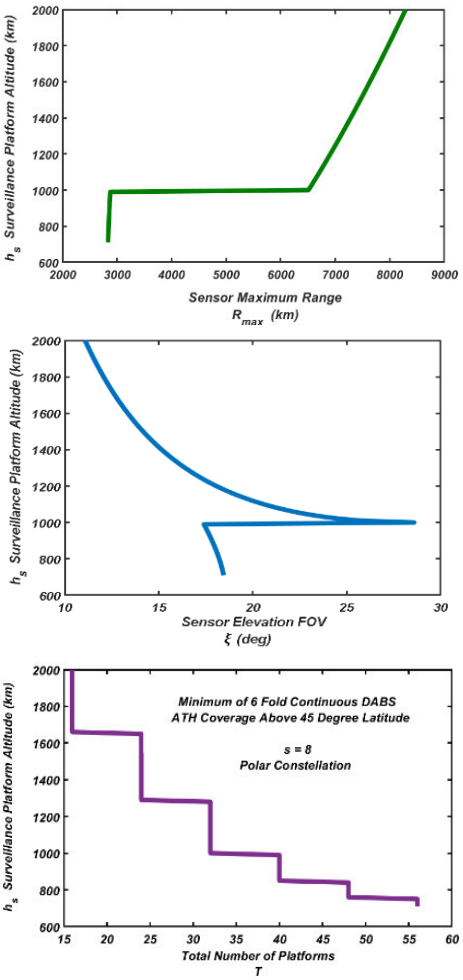

FIGURE 5. Platform altitude as a function of sensor maximum. range, FOV, and total number of platforms.

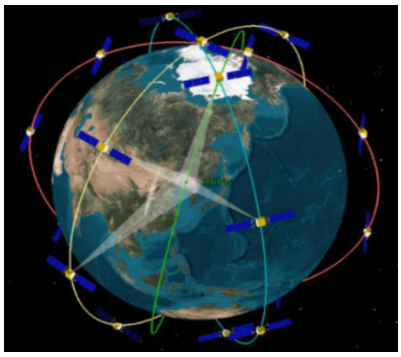

FIGURE 6. Visualization of the proposed optical SBSSN.

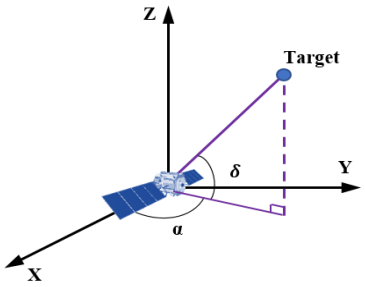

FIGURE 7. Optical sensor measurement schematic.

dual POV method is the preferable choice due to its superior cost-effectiveness ratio [46], [47], [48]. Furthermore, dual POV proves highly effective in addressing the challenging issue of in-orbit initial orbit determination of uncatalogued debris. FIGURE 6 illustrates the designated DABS ATH polar constellation scheme, which offers continuous multiple coverage within the altitude range of 700 to 1000 km around the Earth. Utilizing three polar orbits, each containing eight platforms, the sample target in greet orbit is observed at this moment by four platforms.

The technique for detecting debris through an optical sensor operates as follows: as an object traverses the sensor's FOV within a designated time frame, an image emerges where the object's path is marked by a streak against a background of stationary stars. The object's right ascension and declination angles are computed by extracting information from the stationary stars in the image. As illustrated in FIGURE 7, the object's angular orientation with respect to observation platform is indicated by two angular measurements: right ascension (α) and declination (δ) angles. The measurement models are as described as:

$$\begin{cases} \alpha = tan^{-1}\left(\dfrac{y - y_i}{x - x_i}\right) + \epsilon_1, \\ \delta = tan^{-1}\left(\dfrac{z - z_i}{\sqrt{(x - x_i)^2 + (y - y_i)^2}}\right) + \epsilon_2, \end{cases} \tag{13}$$

here, $[x_i\ y_i\ z_i]^T$ represents the position of j-th sensor in Earth Centered Inertial (ECI) coordinates and $\vec{\epsilon} = [\epsilon_1\ \epsilon_2]^T$ denotes the measurement noise.

Only when the trajectory between the observation platform and the debris avoids atmospheric interaction with Earth, the optical sensor is not pointed at the sun, and the debris is within the FOV of the optical sensor, does a typical LEO space debris become detectable by a space-borne optical sensor. Simulated measurement errors follow a normal distribution pattern, characterized by zero biases and a standard deviation denoted as σ_α for right ascension angles and σ_δ for declination angles, respectively.

C. ESTIMATION ALGORITHM PERFORMANCE EVALUATION

Unscented Kalman Filter (UKF) is applied to estimate the state of the LEO debris using the initial conditions provided in TABLE 1. The dynamic model only takes into account the second zonal harmonic of the Earth, J2, as the perturbation acceleration.

To evaluate the performance of UKF algorithm, three sample LEO debris are selected upon available TLEs, as listed in TABLE 2. As mentioned earlier, the challenge of precise initial orbit determination finds a practical solution by

TABLE 1. Unscented Kalman Filter (UKF) initial conditions. Initial state errors are selected for more than the initial orbit determination accuracies to show the robustness of the estimator.

Dynamic model	Initial state error	$\Delta x_0 = [5\text{ km}; 5\text{ km}; 5\text{ km}; 50\text{ m/s}; 50\text{ m/s}; 50\text{ m/s}]$	
	Process noise matrix	$Q = diag([q_1^2; q_1^2; q_1^2; q_2^2; q_2^2; q_2^2])$ where q_1 is 1e-2, q_2 is 1e-4	
Measurement model	Measurement period	1 second	
	Measurement error	1 arcsecond	
Targets parameters	Ballistic coefficient (upon available TLEs)	Fengyun 1C	0.0001047
		Iridium 33	0.0002466
		Cosmos 2251	0.0002377

TABLE 2. Classical orbital elements of the selected LEO space debris. e, a, i, Ω, ω and *M* represent the eccentricity, semi-major axis, inclination, right ascension of the ascending node, argument of perigee and mean anomaly respectively.

Target	NORAD ID	*e*	*a* (km)	*i* (deg)	Ω (deg)	ω (deg)	*M* (deg)
Fengyun 1C	29779U	0.00645787	7231.791114	98.7667	267.508	349.551	10.4316
Cosmos 2251	34569U	0.0170891	7207.533508	73.9938	202.5972	303.7217	222.086
Iridium 33	33960U	0.0003788	7153.87906	86.271	115.3588	182.2039	225.6781

employing DPOV scheme within a distributed network of space-borne optical sensors [49], [50]. This approach significantly improves the initial orbit determination accuracy due to the increased observability provided by the tracking system. TABLE 3 presents the Gauss angle-only IOD (Initial Orbit Determination) accuracies of the selected targets over 100 Monte Carlo runs for different measurement intervals and SBO (Space-Based Optical) sensors noise levels.

As can be seen, the accuracy of IOD is degraded as the SBO sensor noise becomes larger but even in the case of sensor noise level as much as 10 arcseconds, the results are reasonable.

In all simulations, the accuracy improves as the time intervals increase up to a certain threshold. This enhancement is attributed to the Gauss technique's reliance on the line-of-sight geometry between the target and the observers. As the time interval increases to an optimal value, the configuration becomes more favorable for this technique to produce better results. However, beyond this optimal point, accuracy begins to degrade. The decrease in accuracy occurs because the Gauss technique relies on a simplified two-body problem model and does not consider perturbations.

According to TABLE 3, the mean errors across all cases are minimized when the time interval is set to 120 seconds.

FIGURE 8 displays the average position and velocity errors for Fengyun 1C at three distinct SBO sensor noise levels: 0.1, 1, and 10 arcseconds and TABLE 4, lists the results for all targets. As indicated in TABLE 4, the initial errors for all targets experience a slight increase, with an average factor of 1.1, as the SBO sensor noise levels change from 0.1 to 1 arcseconds. However, when the noise levels increase further from 1 to 10 arcseconds, errors show a significant average increase, with a factor of 2.7. Despite the constraints taken into account for the optical sensors, the consecutive observation time intervals, and hence the performance, remain unaffected.

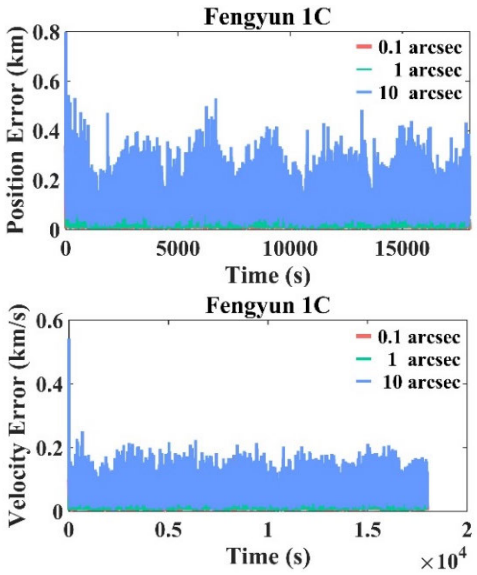

FIGURE 8. Position and velocity errors of Fengyun 1C across different sensor noise levels.

D. LEO DEBRIS ORBIT PREDICTION

Utilizing the identical assumed dynamic model, estimated state of a debris is propagated to desired future epochs, resulting in the generation of prediction errors when compared to the actual recorded orbit. Taking into account the cumulative effects of errors introduced by the assumed dynamic model, measurement process, and estimation process, the prediction error can quickly reach an impractical magnitude as the propagation time increases. We have set a maximum prediction duration of $\Delta t_{prediction}$ equals to seven days (one week) for the simulation. This timeframe is considered sufficient for meeting surveillance and collision avoidance scheduling requirements.

The RSW reference system (radial, along-track, and cross-track) is preferred over ECI to express prediction errors in

TABLE 3. Accuracies of initial orbit determination for selected targets in different scenarios. The "Time Interval" denotes the duration between successive angular measurements. For each target, the Root Mean Squared (RMS) of position and velocity errors under three distinct levels of optical sensor measurement noises is provided.

Target	Time Interval (sec)	Position Error RMS (m)			Velocity Error RMS (m/s)		
		Measurement noise (arcseconds)			Measurement noise (arcseconds)		
		0.1	1	10	0.1	1	10
Fengyun 1C	60	31.84	59.81	414.91	3.04	3.24	22.37
	120	28.83	38.79	350.07	0.64	1.25	7.47
	240	120.59	131.97	749.84	1.41	1.54	8.61
Cosmos 2251	60	56.29	74.41	447.96	2.01	2.72	19.29
	120	43.21	51.15	364.56	0.29	0.75	6.01
	240	82.21	99.71	449.75	0.68	0.95	7.89
Iridium 33	60	168.57	171.41	970.06	2.47	3.48	26.74
	120	39.36	49.56	359.44	0.91	1.62	12.72
	240	353.11	377.28	1462.08	2.52	2.81	13.22

TABLE 4. Performance evaluation of UKF scheme for chosen targets across different sensors noise levels.

Target	Sensor Noise (arcseconds)	Position Error (m)					Velocity Error (m/s)				
		initial	mean	1σ	2σ	3σ	initial	mean	1σ	2σ	3σ
Fengyun 1C	0.1	341.5	16.8	20.2	33.8	55.7	98.7	1.7	1.9	3.3	5.2
	1	356.3	22.9	27.7	46.6	70.3	162.5	2.3	2.6	4.5	7.9
	10	798.8	110.6	130.8	215.1	314.3	538.7	10.1	11.6	18.8	28.4
Cosmos 2251	0.1	223.6	18.2	21.7	37.3	56.5	635.2	2.1	2.1	3.5	8.7
	1	242.5	24.4	28.7	49.2	77.8	791.1	2.7	2.8	5.1	13.6
	10	845.9	115.1	135.2	223.1	325.9	907.6	10.3	11.8	18.9	27.4
Iridium 33	0.1	310.3	18.4	21.3	40.7	62.8	1204.7	3.2	2.1	3.9	17.7
	1	370.8	24.4	28.1	54.3	88.6	1341.3	3.7	2.7	5.2	19.1
	10	1100.5	112.2	129.7	231.3	262.4	1527.1	10.5	11.3	19.1	30.7

future epochs because, as can be observed, it effectively maps the majority of position and velocity error vectors into specific components: the in-track component of the position error vector and the radial component of the velocity error vector, respectively. In RSW coordinates, the Radial axis extends outward from the central body along the line connecting its center to the object in orbit, measuring the distance from the central body. The Along-track axis runs parallel to the object's orbital path, measuring the distance traveled along the orbit. The Cross-track axis is perpendicular to both Radial and Along-track directions, lying within the orbital plane and measuring the distance from the object's orbital path. This coordinate system is valuable for analyzing spacecraft motion and space debris trajectories, providing a concise means to describe positions and velocities in relation to orbital dynamics.

FIGURE 9 illustrates the RSW components of true prediction errors. The horizontal axis represents the prediction interval, while the vertical axis represents position and velocity error components. The primary objective is to minimize the orbit prediction error in the along-track position and radial velocity components.

III. REVIEW OF THE PROPOSE ML APPROACH

In this section, a concise introduction to the proposed PCA-SVM regression model is presented.

A. SUPPORT VECTOR MACHINE

SVM regression, a supervised learning algorithm, is employed for solving regression tasks involving the prediction of continuous numerical values. This technique addresses regression challenges through the incorporation of kernel functions, enabling the model to capture complex nonlinear relationships within the dataset. SVM regression's primary objective is to identify a hyperplane in a higher-dimensional feature space that best fits the data points. The pivotal concept behind achieving this goal is the "kernel trick". Instead of explicitly transforming the data into the higher-dimensional space, SVM regression applies kernel functions to compute inner products among data points in the higher-dimensional space, all without needing to explicitly represent the data. This approach significantly reduces computational complexity while retaining the capability to capture non-linear patterns.

The Gaussian kernel is preferred in this study due to its ability to facilitate non-linear transformations, possess the universal approximation property, and generate smooth decision boundaries. It calculates the similarity between two data points, often referred to as support vectors. For two data points, $\boldsymbol{x_i}$ and $\boldsymbol{x_j}$, the Gaussian kernel function is given by:

$$K(\boldsymbol{x_i}, \boldsymbol{x_j}) = exp(-\gamma \left\| \boldsymbol{x_i} - \boldsymbol{x_j} \right\|^2), \tag{14}$$

where $\left\| \boldsymbol{x_i} - \boldsymbol{x_j} \right\|$ represents the Euclidean distance between the feature vectors of $\boldsymbol{x_i}$ and $\boldsymbol{x_j}$, and γ serves as a hyperparameter, kernel scale, that controls the width of the Gaussian kernel. Smaller γ values result in a wider Gaussian curve, while larger γ values lead to a sharper curve.

SVM regression formulates the problem as a convex optimization task, aiming to minimize the loss function and maximize the margin through a combination of loss and

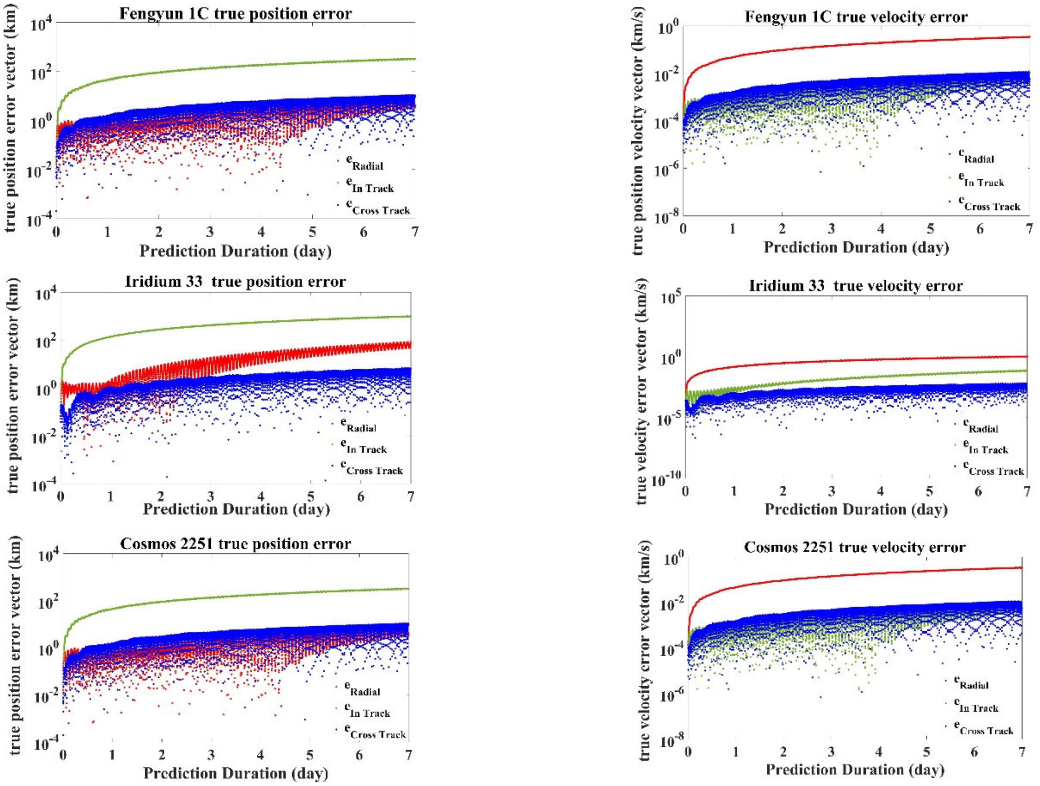

FIGURE 9. Radial, in-track and cross-track components of position and velocity error in one week orbit prediction for selected targets.

regularization. Typically, the selected loss function is the epsilon-insensitive loss, which permits a specified deviation (ε) between the predicted and actual target values. It can be expressed as:

$$\begin{aligned}
&\text{Minimize}: \; L\left(w, b, \xi, \xi^*\right) = \frac{1}{2}\|w\|^2 + C\sum_{i=1}^{n}\left(\xi_i + \xi_i^*\right), \\
&\text{Subject to: } \phi y_i - w^T(x_i) + b \le \varepsilon + \xi_i, \\
&\qquad \phi(w^T(x_i) + b) - b \le \varepsilon + \xi_i^*, \\
&\qquad \xi_i, \xi_i^* \ge 0, \qquad (15)
\end{aligned}$$

where w is the weight vector that defines the decision boundary of the SVM regression model and b is the bias term that shifts the decision boundary. ξ_i and ξ_i^* are non-negative slack variables associated with each training example i and represent the amount by which each data point can violate the epsilon-insensitive loss. C is the regularization parameter and controls the trade-off between minimizing the regularization term and minimizing the sum of slack variables. Higher values of C emphasize fitting the training data well, while lower values encourage a larger margin and more emphasis on regularization. $\phi(\boldsymbol{x_i})$ represents the transformation of the input data $\boldsymbol{x_i}$ into a higher-dimensional feature space using the Gaussian kernel and n is the number of training examples.

In Eq. (15), the first term represents the regularization term, promoting a balance between maximizing the margin and minimizing the magnitude of the weight vector w. The second term represents the sum of slack variables, penalized by the regularization parameter C, and governs the trade-off between fitting the training data and allowing errors within the epsilon (ε) range. The optimization problem seeks to find the values of w, b, ξ_i, ξ_i^* that minimize the objective function while satisfying these constraints, ultimately finding the best hyperplane for regression while allowing for a margin of error defined by ε.

Lagrange dual formulation is applied to efficiently solve the SVM regression optimization problem. The Lagrange multipliers (α_i, α_i^*) associated with each data point represent the importance of that data point as a support vector. The dual problem seeks to maximize the Lagrangian while respecting the constraints. Solving the dual problem yields the optimal values of α_i and α_i^* according to:

$$\begin{aligned}
&\text{Minimize}: \; L\left(\alpha_i, \alpha_i^*\right) \\
&\qquad = \frac{1}{2}\sum_{i=1}^{n}\sum_{i=1}^{n}\left(\alpha_i - \alpha_i^*\right)\left(\alpha_j - \alpha_j^*\right) K\left(\boldsymbol{x_i}, \boldsymbol{x_j}\right) \\
&\qquad + \varepsilon\sum_{i=1}^{n}\left(\alpha_i + \alpha_i^*\right) \\
&\qquad - \sum_{i=1}^{n}\left(\alpha_i - \alpha_i^*\right) y_i. \\
&\text{Subject to: } \sum_{i=1}^{n}\left(\alpha_i - \alpha_i^*\right) = 0, \\
&\qquad 0 \le \alpha_i, \quad \alpha_i^* \le C. \qquad (16)
\end{aligned}$$

The decision function in SVM regression is expressed as a weighted sum of kernel evaluations for support vectors as:

$$f(\boldsymbol{x}) = \sum_{i=1}^{n}\left(\alpha_i - \alpha_i^*\right) K\left(\boldsymbol{x}_i, \boldsymbol{x}\right) + b, \qquad (17)$$

where $K(\boldsymbol{x}_i, \boldsymbol{x})$ represents the kernel value between the support vector $\boldsymbol{x}_i$ and the input data $\boldsymbol{x}$ respectively.

B. PRINCIPAL COMPONENT ANALYSIS

PCA is a dimensionality reduction technique used to transform a dataset with potentially correlated variables into a new set of uncorrelated variables, known as principal components. These components capture the data's most notable patterns of variation, which facilitates the visualization, analysis, and comprehension of complicated datasets. Mathematically, PCA involves several key steps. First the data is mean-centered by subtracting the mean of each feature from every data point according to:

$$\begin{aligned} \boldsymbol{x}_{mean} &= \frac{1}{n}\sum_{i=1}^{n} \boldsymbol{x}_i, \\ \boldsymbol{x}'_i &= \boldsymbol{x}_i - \boldsymbol{x}_{mean}, \end{aligned} \tag{18}$$

where n is the number of data points, $\boldsymbol{x_i}$ represents the original data for i-th feature, $\boldsymbol{x'_i}$ represents the mean-centered data.

Then, the covariance matrix of the centered data is computed as:

$$C_{ij} = \frac{1}{n-1}\sum_{k=1}^{n}(\boldsymbol{x'_{ik}} - \boldsymbol{x}_{mean})(\sum_{k=1}^{n}(\boldsymbol{x'_{jk}} - \boldsymbol{x}_{mean}), \tag{19}$$

where C_{ij} represents the covariance between $\boldsymbol{x'_i}$ and $\boldsymbol{x'_j}$.

Next, eigenvalue decomposition is performed on the covariance matrix to find the eigenvalues (λ_i) and corresponding eigenvectors $(\boldsymbol{e_i})$ for $i = 1, 2, \ldots, n$.

The eigenvalues indicate the variance explained by each eigenvector. Eigenvalues are sorted in descending order $\{\lambda'_1\lambda_2 \ldots \lambda_n\}$ so that $\lambda_1 > \lambda_2 > \ldots > \lambda_n$. The variance explained by each component is given by:

$$\sigma_{explained.i} = \frac{\lambda_i}{\sum_{i=1}^{p}\lambda_i}, \tag{20}$$

where p is the number of features in the original dataset. The total variance retained by 'k' components is determined from:

$$\sigma_{total,retained} = \sum_{i=1}^{k}\sigma_{explained,i}, \tag{21}$$

to reduce the dimensionality, the top 'k' eigenvectors are selected based on the largest eigenvalues and their corresponding principal components PC_i are computed from:

$$PC_i = \boldsymbol{e_i} \cdot \boldsymbol{x}'. \tag{22}$$

By retaining the top principal components that explain most of the variance, and projecting the dataset onto them, PCA effectively reduces the dimensionality of the data, making it easier to interpret while retaining crucial information.

IV. DATASET CONSTRUCTION

This section outlines the methodology for designing the dataset structure for the proposed PCA-SVM approach. The establishment of a meaningful relationship between the learning and target variables in the dataset is of paramount importance, as it enables the ML model to effectively capture relevant patterns. However, due to the absence of a comprehensive theory that addresses unmodeled hidden relationships, the design procedure relies on a trial-and-error approach. To validate the results of the ML approach and evaluate its generalization capability, the test data is kept entirely separate from the training data and is not used in the training process. Additionally, the dataset structure must allow for access to both the learning and target variables during the learning process, while ensuring that the learning variables remain accessible during the modification process. Prior to delving into the construction of the learning dataset utilized in this study, several notations are introduced for simplification. The symbol $X(t)$ represents the orbit state at the desired epoch, and the superscript signifies the coordinate frame used to express $X(t)$, including options such as Classical Orbit Elements (COE), ECI, and RSW frames. $X_{COE}\ (t) = [a,\ e,\ i, \Omega, \omega\ ,\ M]$ represents the classical orbital elements, while $X_{ECI}(t) = [x,\ y,\ z,\ v_x,\ v_y,\ v_z]$ corresponds to the ECI frame. Similarly, $X_{RSW}(t)$ represents the components of position and velocity vectors in RSW frame. $X_{true}(t)$ denotes the actual orbit at epoch t, whereas $X_{est}(t)$signifies the estimated orbit at the same epoch. Additionally, $X_{prop}(t_i,\ t_j)$ represents the predicted orbit at epoch t_i based on the estimated orbit $X_{est}(t_j)$, where $(t_i > t_j)$. The calculation of the true orbit prediction error, denoted as e(t), is as follows:

$$e\left(t_j\right) = X_{true}\left(t_i\right) - X_{prop}\left(t_i, t_j\right). \tag{23}$$

Potential sources of information contributing to orbit prediction errors can be found within the learning variables listed in TABLE 5.

This study considers six target variables that correspond to the position and velocity components of error vector. These variables are denoted as $\{e_{Rradial},\ e_{Rin-track}, e_{Rcross-track}, e_{Vradial} e_{Vin-track}, e_{Vcross-track}\}$. The dataset is divided into the standard practice of 75% training data and 25% test data. The training data is employed for training the SVM regression model, optimizing its parameters, and identifying the optimal hyperplane for data fitting. The remaining 25% is reserved as an independent test set, used to assess the model's performance on unseen data. This approach ensures a fair assessment of the model's ability to generalize to new data and provides valuable insights into its real-world effectiveness.

Moreover, PCA was applied to normalized feature space to reduce its dimensionality and capture the most significant variations in the data.

PCA transforms the original features into a new orthogonal coordinate system, where the first principal component explains the largest variance, the second explains the second largest variance, and so on.

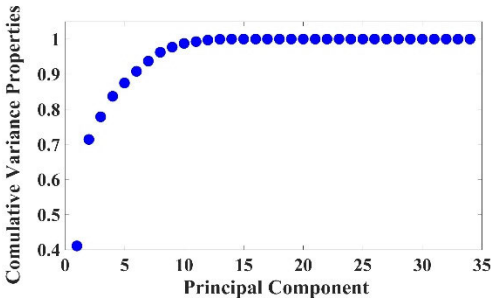

FIGURE 10. Accumulated variance in PCA analysis.

As shown in FIGURE 10, by selecting the top 10 principal components, approximately 99% of most important patterns in the data are retained, reducing computational complexity and potential noise from less informative features.

In SVM regression, hyper-parameters are parameters that are set prior to the training process and cannot be directly learned from the data. They play a crucial role in configuring and fine-tuning the SVM regression model and significantly affect the model's performance. Consequently, they must be carefully selected to achieve optimal results.

The term ''optimal hyper-parameters'' refers to the values of these parameters that result in the best performance of the SVM regression model on a given dataset. Determining the optimal hyper-parameters is crucial for achieving high accuracy and generalization ability of the SVM regression model.

The key hyper-parameters include ''Kernel Scale'' which determines the width of influence of the Gaussian kernel on the predictions. ''Box Constraint'' constraints the magnitude of the Lagrange multipliers and affect the model's complexity and potential overfitting. Finally, ''Epsilon'' parameter controls the tolerance level for the epsilon-insensitive loss function, allowing predictions within a certain range of actual target value. During hyper-parameter optimization, different combinations of these values are explored through techniques like grid search or random search, along with cross-validation to find the most effective set of hyper-parameters.

V. PCA-SVM REGRESSION SIMULATION RESULTS

This section presents numerical results in four subsections, each focusing on different aspects. The evaluation begins with an assessment of the learning capability exhibited by the PCA-SVM model. Subsequently, the effects caused by optical sensor noise are examined. Then, the model's maximum prediction capacity is explored. Lastly, the impact of noise and randomness on the system is investigated. To establish the SVM model, the SVM regression function in MATLAB is utilized, with a summary of employed parameters provided in section IV. It should be mentioned that the performance of the developed model was evaluated on the test data using the four following metrics:

$$RMSE = \sqrt{\frac{1}{n}\sum_{i=1}^{n}(y_i - \hat{y}_i)^2}, \tag{24}$$

$$MaxErr = \max(|y_i - \hat{y}_i|), \tag{25}$$

$$MAE = \frac{1}{n}\sum_{i=1}^{n}|y_i - \hat{y}_i|, \tag{26}$$

$$R2 = 1 - \frac{\sum_{i=1}^{n}(y_i - \hat{y}_i)^2}{\sum_{i=1}^{n}(y_i - \bar{y})^2}, \tag{27}$$

where y_i represents true value of the i-th data point, $\hat{y}_i$ is the ML-predicted value of i-th data point, $\bar{y}$ is the mean value of all train data points. Root Mean Squared Error (RMSE) measures the average magnitude of the difference between the predicted and actual target values. Mean Absolute Error (MAE) calculates the average absolute difference between the predicted and actual target values. Maximum Error (MaxErr) determines the largest absolute difference between the predicted and actual target values, while the R2 score evaluates the proportion of variance in the dependent variable that can be explained by the model.

A. LEARNING CAPABILITY OF PCA-SVM REGRESSION APPROACH

The optical DABS constellation is capable of real-time debris monitoring, as exemplified in FIGURE 8 and TABLE 4.

In the dataset preparation process, for each target specified in TABLE 2, a total of eight distinct estimated epochs are selected. Among these epochs, four are associated with optical sensor noise of 1 arcseconds, and the other four are tied to optical sensor noise of 5 arcseconds. Using the estimated state vectors obtained from the selected epochs, the trajectory of debris is simulated and propagated for a duration of one week. For every specific optical sensor error scenario, three epochs are selected, along with their corresponding variables, to construct the training dataset.

Furthermore, one epoch is designated as the test dataset, enabling a comprehensive evaluation of the model's performance. Total debris training dataset then underwent training for six distinct models, each dedicated to compensating the components of position and velocity error vectors.

TABLE 6 presents the optimal hyper-parameters achieved during the training phase of all six models. The hyper-parameters were obtained using the SMO algorithm, implemented in MATLAB.

FIGURE 11 illustrates the evaluation of objective function during the optimization of hyper-parameters for the two models associated with the dominant errors of position and velocity error vectors, $R_{intrack}$ and V_{radial} respectively. The objective function serves as a metric for assessing the performance of the optimization process and ensuring that the models achieve their optimal configurations with respect to the specified hyper-parameters.

B. EVALUATING DIFFERENT OPTICAL SENSOR NOISE LEVELS

In this subsection, a study is undertaken to analyze the robustness of the robustness of the proposed PCA-SVM regression technique in the face of optical sensor noise. The examination

TABLE 5. Selected learning variables in SVM regression.

Variable Number	Symbol	Name
1	ε	measurement noise of on-board optical sensor
2-7	$X_{est}^{ECI}(t_j)$	current estimation of the orbit state expressed in ECI frame
8-13	$X_{est}^{COE}(t_j)$	current estimation of the orbit state expressed in COE format
14	Δt	prediction duration
15	$n_{kfold}(t_j)$	coverage multiplicity of the optical SSN at current estimation time
	$(\alpha,\delta)_{t_j,min}$	Minimum of optical observations at current estimation
16-21	$(\alpha,\delta)_{t_j,max}$	Maximum of optical observations at current estimation
	$(\alpha,\delta)_{t_j,avg}$	Average of optical observations at current estimation
22-27	$X_{prop}^{ECI}(t_i)$	prediction of the orbit state to future epoch t_i expressed in ECI frame
28-33	$X_{prop}^{COE}(t_i)$	prediction of the orbit state to future epoch t_i expressed in COE format

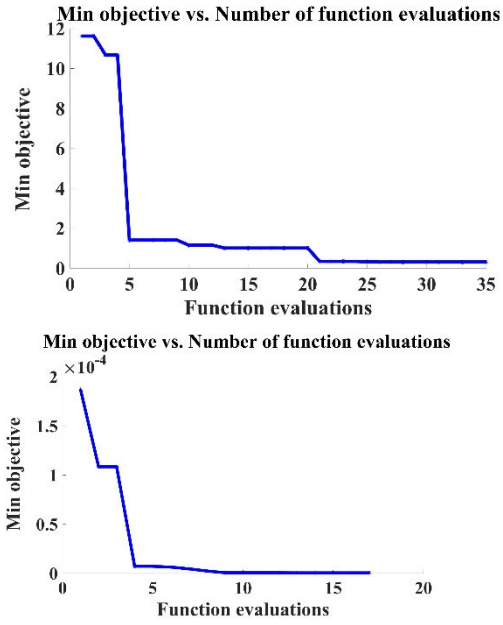

FIGURE 11. Evaluation of objective functions $R_{in-track}$ model and V_{radial} model for hyper-parameters optimization.

TABLE 6. Optimal hyper-parameters for the proposed PCA-SVM regression.

SVM Model	Max Iteration	Objective	Box Constraint	Kernel Scale	Epsilon
R_{radial}	35	0.0059961	969.72	3.1919	0.05453
$R_{in\,track}$	35	0.3068	989.03	2.1653	0.38002
$R_{cross\,track}$	35	0.014235	990.06	1.7133	0.10063
V_{radial}	17	3.781e-07	114.22	1.7969	0.001066
$V_{in\,track}$	17	4.766e-07	218.23	51.332	8.2944e-06
$V_{cross\,track}$	17	6.685e-08	895.33	42.217	0.00022971

is conducted for two distinct cases, where the noise levels are set at 1 and 5 arcseconds.

1) OPTICAL SENSOR NOISE LEVEL AT 1 ARCSECOND

FIGURE 12 and FIGURE 13 display the performance of all six models within the proposed PCA-SVM regression ML approach, using Fengyun 1C debris as an example. FIGURE 12 is associated with the RSW components of position error, whereas FIGURE 13 pertains to the RSW components of velocity error. They illustrate how well the models predict the behavior of Fengyun 1C debris, offering insights into their effectiveness in capturing patterns and trends within the dataset. A set of three graphs accompanies each model to evaluate its performance. The first graph displays the residual error plotted against the predicted values obtained from the ML model. This gives insights into how well the model's predictions align with the actual data. The second graph compares the true values and the predicted values generated by the ML model.

By analyzing this graph, researchers can assess the accuracy of the ML model's predictions and identify any discrepancies. Lastly, the third graph shows the true prediction error, the ML-predicted error, and the residual error within a one-week timeframe. This plot enables a detailed examination of the model's performance in capturing variations and deviations from the actual data within the specified time frame. Together, these three graphs comprehensively evaluate each ML model's capabilities. As previously stated, it is evident from the FIGURE 9 that the primary sources of error for position and velocity are the in-track component of position error and the radial component of velocity error, respectively. Thus, the focus will be on presenting the results corresponding to these dominant errors for the remainder of the simulation. TABLE 7 presents a detailed performance evaluation of each PCA-SVM regression model across various targets associated with optical sensors' error of 1 arcsecond.

2) OPTICAL SENSOR NOISE LEVEL AT 5 ARCSECONDS

FIGURE 14 illustrates the performance of PCA-SVM regression models corresponding to dominant errors of position and velocity of Fengyun 1C as an example. TABLE 7 presents a detailed performance evaluation of each PCA-SVM regression model across various targets associated with optical sensors' error of 5 arcseconds.

As evident from TABLE 7 and TABLE 8, it is not consistently true that the prediction error increases with larger

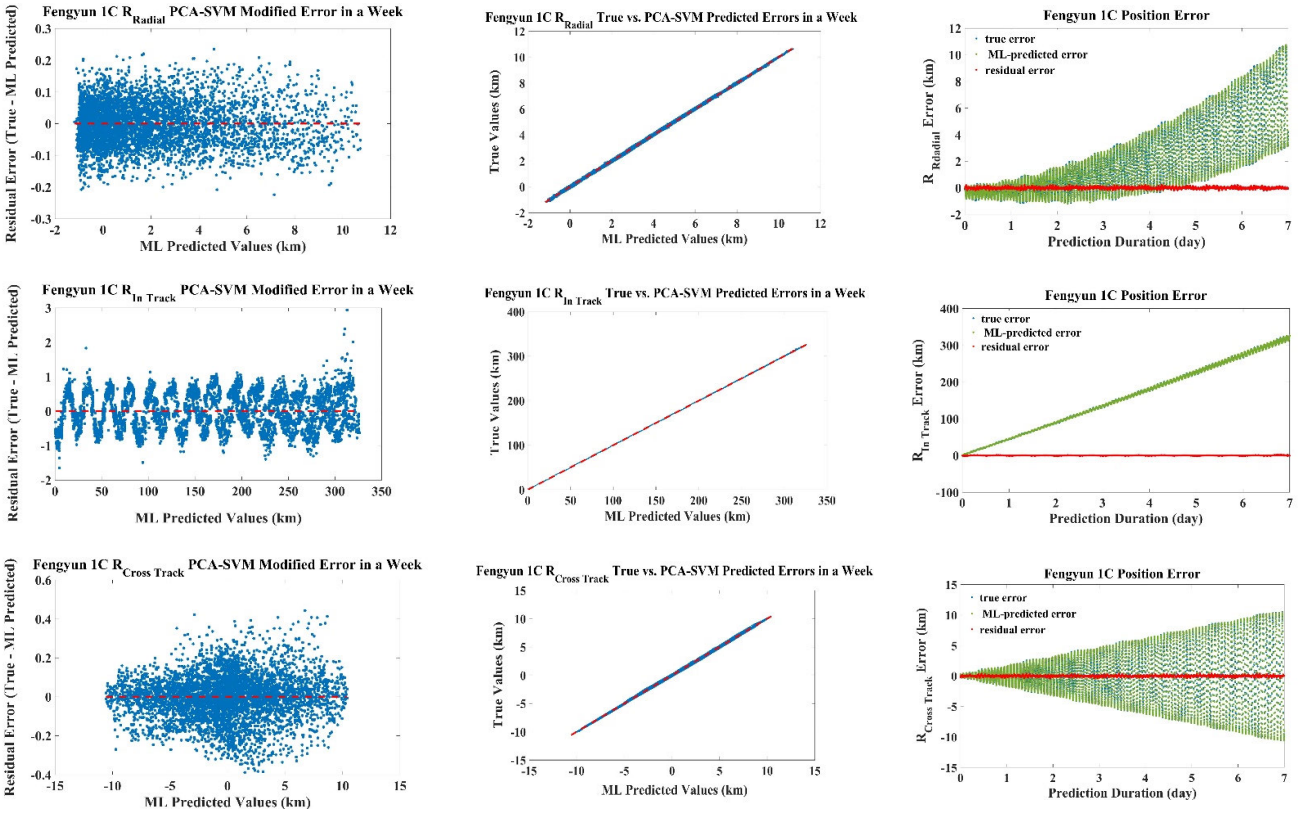

FIGURE 12. Performance evaluation of the PCA-SVM regression models on enhancing components of Fengyun 1C position error vector under 1 arcseconds sensor noise level.

TABLE 7. Performance evaluation of PCA-SVM regression models considering optical sensor error of 1 arcsecond. Errors are expressed in km and km/s respectively.

		R2 score	RMSE	MAE	MaxErr
Fengyun 1C	R_{radial}	0.9994	0.0683	0.0549	0.2351
	$R_{in\ track}$	0.9999	0.5154	0.4405	2.9309
	$R_{cross\ track}$	0.9993	0.1159	0.0882	0.4418
	V_{radial}	0.9999	6.4827e-04	5.3581e-04	0.0037
	$V_{in\ track}$	0.9521	7.4611e-04	6.0218e-04	0.0016
	$V_{cross\ track}$	0.9743	7.4567e-04	5.9859e-04	0.0018
Cosmos 2251	R_{radial}	0.9999	0.0854	0.0701	0.2785
	$R_{in\ track}$	0.9999	0.6543	0.5242	6.1524
	$R_{cross\ track}$	0.9982	00.1238	0.1003	0.4017
	V_{radial}	0.9999	0.0011	8.9113e-04	0.0049
	$V_{in\ track}$	0.9989	4.9368e-04	4.0061e-04	0.0015
	$V_{cross\ track}$	0.9718	5.4653e-04	4.6626e-04	0.0016
Iridium 33	R_{radial}	0.9996	0.0679	0.0541	0.2706
	$R_{in\ track}$	0.9999	0.5856	0.4727	6.8259
	$R_{cross\ track}$	0.9992	0.1233	0.0940	0.7135
	V_{radial}	0.9999	8.4721e-04	6.6957e-04	0.0051
	$V_{in\ track}$	0.9628	6.9091e-04	5.5714e-04	0.0019
	$V_{cross\ track}$	0.9737	7.3702e-04	5.9097e-04	0.0018

sensor noise levels. As mentioned earlier, the accuracy of estimated state at a specific epoch and the instantaneous coverage multiplicity of the target seems to influence the prediction error. For instance, in the case of Fengyun 1C, in the case of 5 arcseconds optical sensor noise, the coverage multiplicity for the corresponding epoch is 3, while for the 5 arcseconds sensor noise at the corresponding epoch, it increases to 8, resulting in a reduction of prediction error for this particular scenario. This observation emphasizes the importance of considering these factors while interpreting the prediction results for different sensor noise levels.

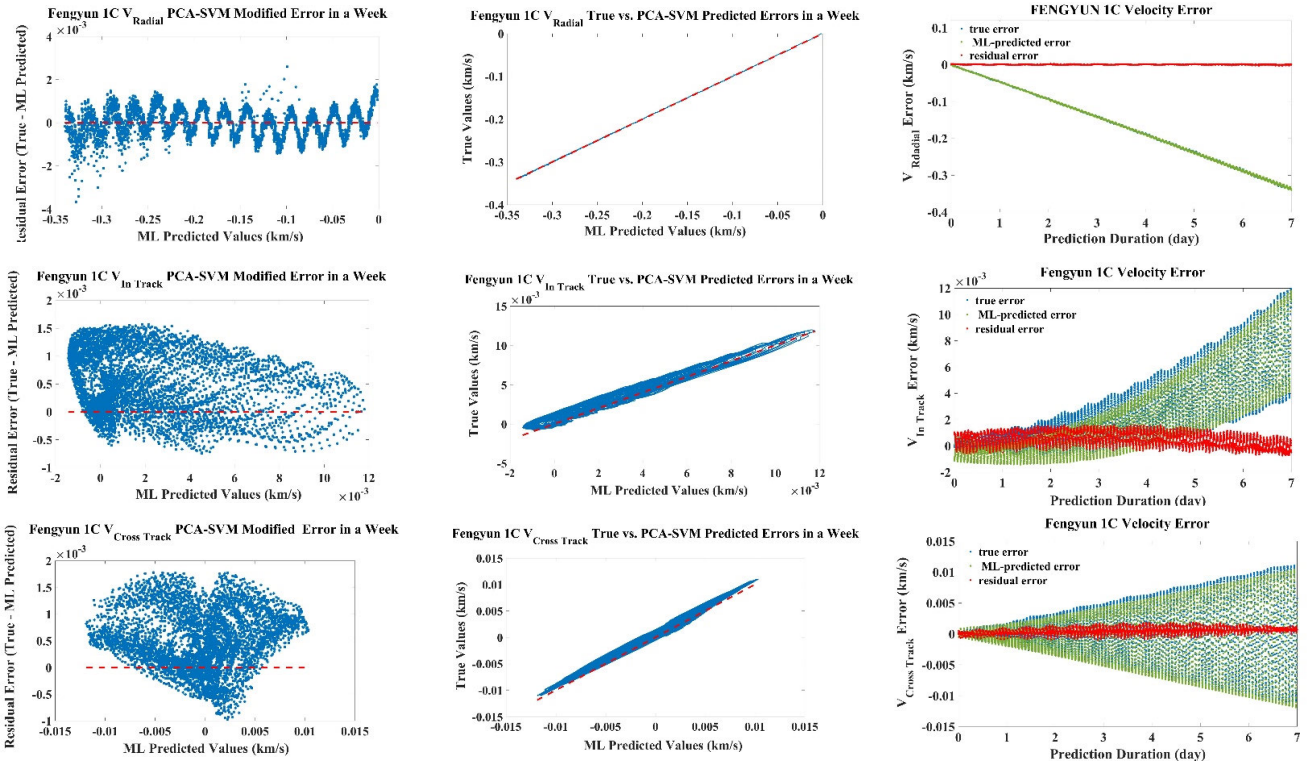

FIGURE 13. Performance evaluation of the PCA-SVM regression models on enhancing components of Fengyun 1C velocity error vector under 1 arcseconds sensor noise level.

TABLE 8. Performance evaluation of PCA-SVM regression models on targets considering optical sensor error of 5 arcseconds. Errors are expressed in km and km/s.

		R2 score	RMSE	MAE	MaxErr
Fengyun 1C	R_{radial}	0.9976	0.0708	0.0573	0.2601
	$R_{in\ track}$	0.9998	0.5329	0.4620	1.1189
	$R_{cross\ track}$	0.9996	0.1117	0.0849	0.4195
	V_{radial}	0.9998	5.2431e-04	4.5226e-04	0.0012
	$V_{in\ track}$	0.8530	8.6692e-04	8.3349e-04	0.0016
	$V_{cross\ track}$	0.9889	5.7284e-04	4.7985e-04	0.0018
Cosmos 2251	R_{radial}	0.9999	0.0899	0.0743	0.6497
	$R_{in\ track}$	0.9999	0.7612	0.5703	7.9554
	$R_{cross\ track}$	0.9981	0.1188	0.0964	0.3988
	V_{radial}	0.9999	0.0013	9.5911e-04	0.0070
	$V_{in\ track}$	0.9962	0.0014	0.0012	0.0041
	$V_{cross\ track}$	0.9616	5.0085e-04	4.1996e-04	0.0016
Iridium 33	R_{radial}	0.9989	0.0850	0.1085	0.7819
	$R_{in\ track}$	0.9998	0.6546	0.6148	11.601
	$R_{cross\ track}$	0.9983	0.1229	0.1019	0.4507
	V_{radial}	0.9998	1.7835e-04	8.3066e-04	0.0081
	$V_{in\ track}$	0.9917	1.2743e-04	1.1815e-04	0.0049
	$V_{cross\ track}$	0.9726	5.1237e-04	5.7108e-04	0.0015

C. NOISY DATA

This section explores the impact of randomness and noise within the dataset. The objective of the SVM model is to accurately capture the underlying relationship between the original learning and target variables in the learning process.

In noise-free test dataset conditions, SVM model performs well, with results presented in TABLE 7 and TABLE 8 confirming the effectiveness of the PCA-VM regression model, as evident in FIGURE 12 to FIGURE 14.

Effectiveness is reasonable due to the PCA-SVM model's primary task of capturing patterns from the original noise-free dataset. As a data-driven algorithm, the PCA-SVM model encounters c However, when random noise is introduced to one percent of the entire dataset, with all features augmented

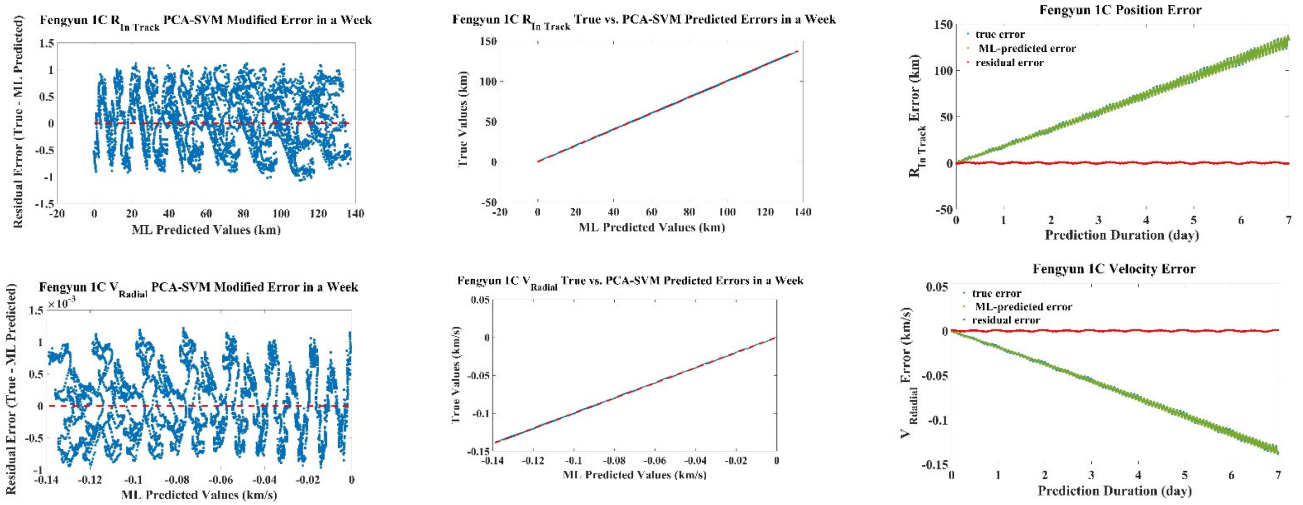

FIGURE 14. Performance assessment of PCA-SVM regression for dominant position and velocity errors of Fengyun 1C with optical sensor level of 5 arcseconds.

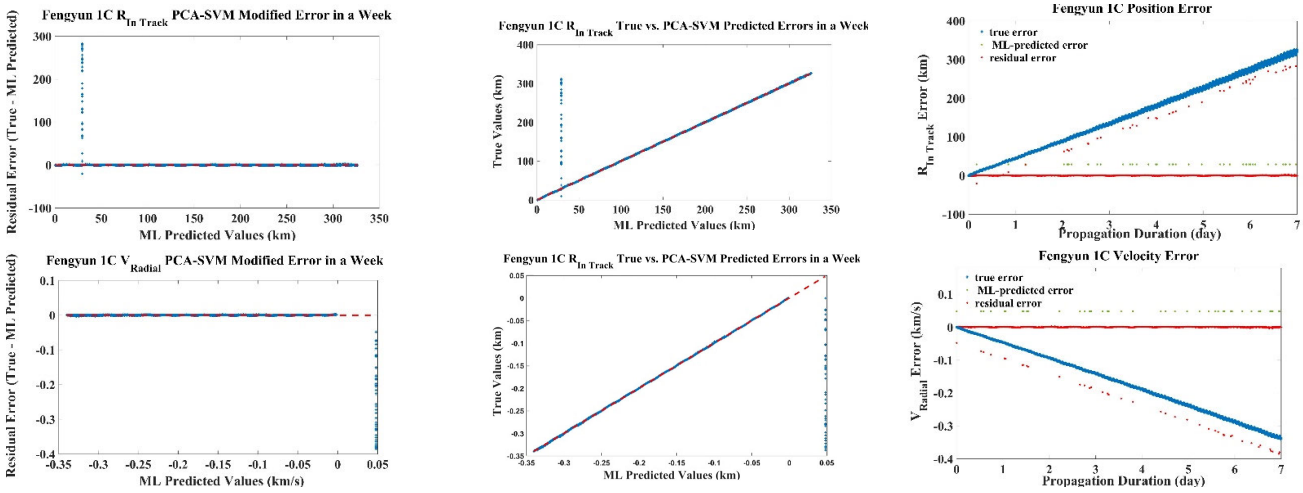

FIGURE 15. Impact of noise on the performance of PCA-SVM regression models for Fengyun 1C with 1 arcsecond optical sensor noise.

by Gaussian noise having a mean of 0 and a variance equal to 0.1 times their original values, the performance of the trained model significantly deteriorates. The decline in model performance is clearly depicted in FIGURE 15 and FIGURE 16. This observed drop in model challenges when predicting accurate outputs in the presence of datasets containing noisy features. Therefore, model's inability to handle noisy features justifies the decrease in performance under such conditions. When the test dataset is not noisy, the performances of the trained PCA-SVM model are shown in TABLE 7 and TABLE 8. In this case, as illustrated in FIGURE 12 to FIGURE 14, the PCA-SVM regression model works well. In another case, random noise is added to one percent of the whole dataset in such a way that all the features are added to a Gaussian noise of mean 0 and variance equal to 0.1 times of their original values. As illustrated in FIGURE 15 and FIGURE 16, the performance of the trained model exhibits limitations, as SVM model is supposed to capture the pattern of the original dataset without any noise introduced. This result because the SVM model is expected to capture the pattern of the original dataset without any added noise. Given that ML algorithms are fundamentally data-driven, the model faces challenges in accurately predicting the output when confronted with noisy data.

TABLE 9 presents a detailed performance evaluation of PCA-SVM regression model across various targets associated with noisy data.

D. EXTEND PREDICTION TIME

In this section, the time span of ML-modification is explored, referring to the maximum future interval within which the trained SVM model can effectively reduce the orbit prediction error. The findings will demonstrate that there are constraints

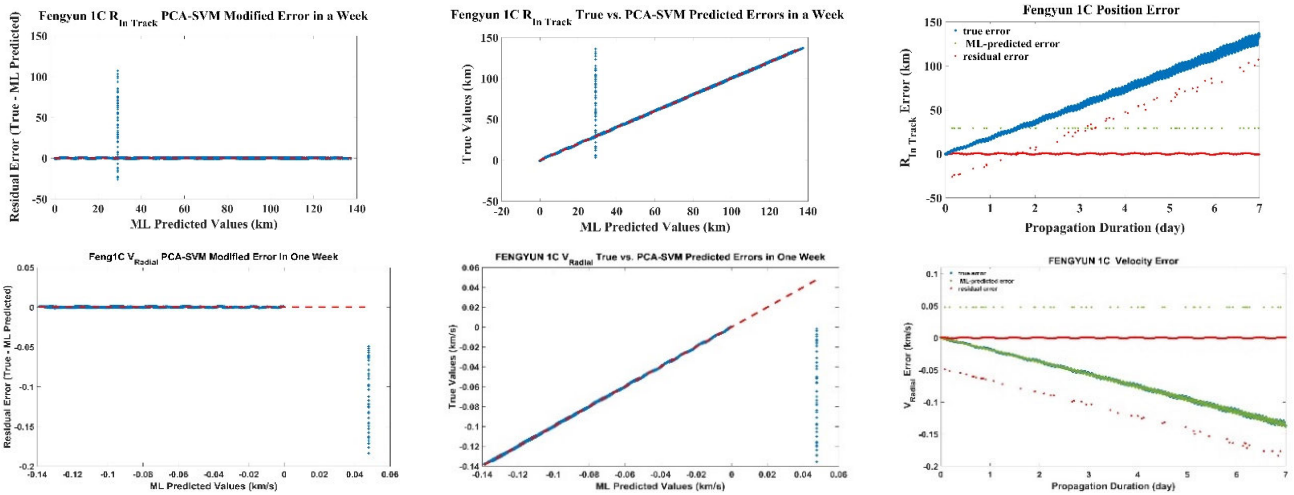

FIGURE 16. Impact of noise on the performance of PCA-SVM regression models for Fengyun 1C with 5 arcseconds optical sensor noise.

TABLE 9. Performance evaluation of PCA-SVM approach in the presence of noisy data with varied optical sensor noise levels. Errors are expressed in km and km/s.

LEO Debris	Optical sensor error	Error component	R2 score	RMSE	MAE	MaxErr
Fengyun 1C	1 arcseconds	$R_{in\ track}$	0.9626	17.8873	1.9725	282.5943
		V_{radial}	0.9343	0.0250	0.0027	0.3852
	5 arcseconds	$R_{in\ track}$	0.9768	5.8071	0.9795	106.9751
		V_{radial}	0.9034	0.0122	0.0016	0.1836
Cosmos 2251	1 arcseconds	$R_{in\ track}$	0.9591	48.5711	4.7841	866.6062
		V_{radial}	0.9655	0.0461	0.0049	0.8258
	5 arcseconds	$R_{in\ track}$	0.9737	45.9489	3.8965	916.5603
		V_{radial}	0.9614	0.0576	0.0057	1.0213
Iridium 33	1 arcseconds	$R_{in\ track}$	0.9497	24.8165	2.6725	406.6146
		V_{radial}	0.9756	0.0182	0.0022	0.3518
	5 arcseconds	$R_{in\ track}$	0.9694	16.1803	1.7020	293.4832
		V_{radial}	0.9464	0.0226	0.0026	0.3843

TABLE 10. Performance evaluation of trained PCA-SVM approach over a 10-day duration under diverse sensor error levels. Errors are expressed in km and km/s.

LEO Debris	Optical sensor error	Error vector component	R2 score	RMSE	MAE	MaxErr
Fengyun 1C	1 arcsecond	$R_{in\ track}$	0.9970	4.9868	3.3780	26.6268
		V_{radial}	0.9961	0.0059	0.005	0.0139
	5 arcseconds	$R_{in\ track}$	0.9968	3.1086	1.6322	12.3816
		V_{radial}	0.9998	0.000788	0.00061	0.0033
Cosmos 2251	1 arcsecond	$R_{in\ track}$	0.9953	2.5811	1.5641	22.1377
		V_{radial}	0.9863	0.000976	0.0091	0.0061
	5 arcseconds	$R_{in\ track}$	0.9967	6.2905	3.8823	33.5175
		V_{radial}	0.9962	0.0029	0.002	0.0057
Iridium 33	1 arcsecond	$R_{in\ track}$	0.9974	4.3933	1.6274	15.1531
		V_{radial}	0.9908	0.000913	0.00095	0.0074
	5 arcseconds	$R_{in\ track}$	0.9959	5.3013	4.3180	31.1760
		V_{radial}	0.9957	0.0032	0.007	0.0175

on the correction capability. An analysis of the trained PCA-SVM regression method using the representative sample Fengyun 1C is shown in FIGURE 17 and FIGURE 18. Instead of the prior one-week timeframe, the research extends the observation period to two weeks while taking into account optical sensor noise levels of 1 arcsecond and 5 arcseconds, respectively. The results documented in presents the model's performance across various targets under different sensor noise levels. For each model, the presentation features two graphs. One graph depicts the model's performance over a two-week prediction duration, while the other illustrates its performance during the second week, despite the model being trained with a one-week prediction duration limit. As evident from the TABLE 10 and FIGURE 18., the

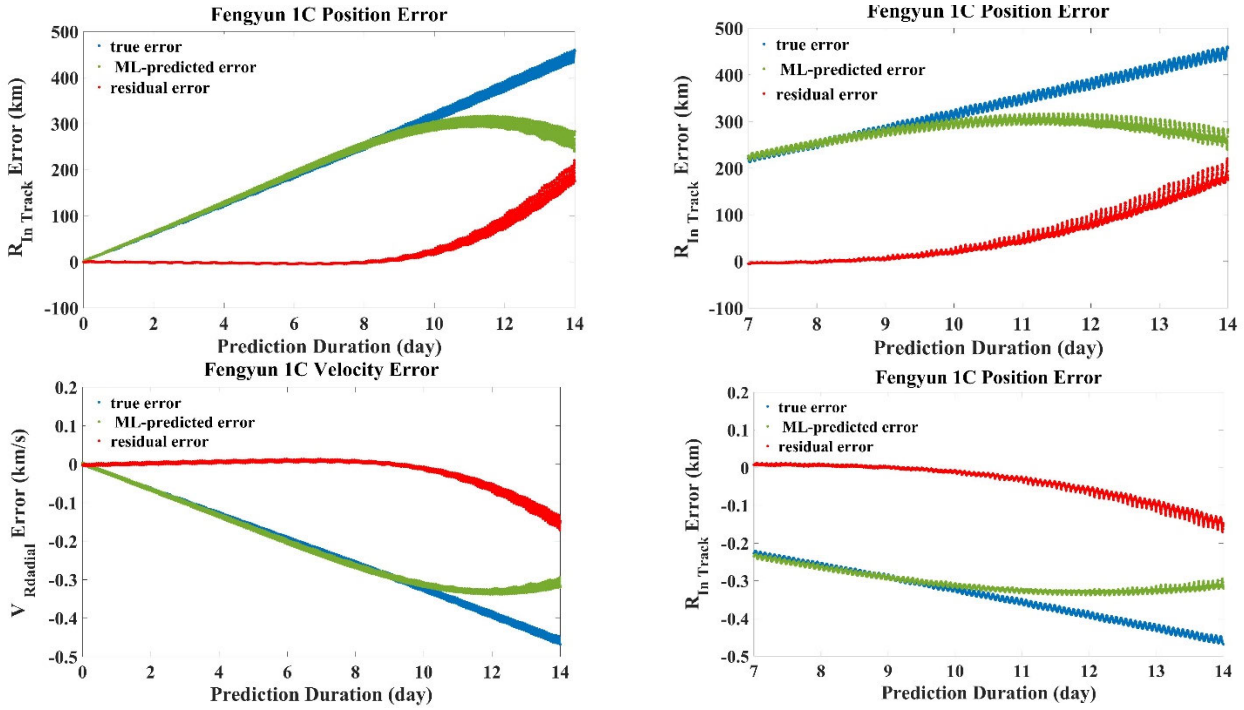

FIGURE 17. Assessment of PCA-SVM regression performance on Fengyun 1C with 1 arcsecond optical sensor error.

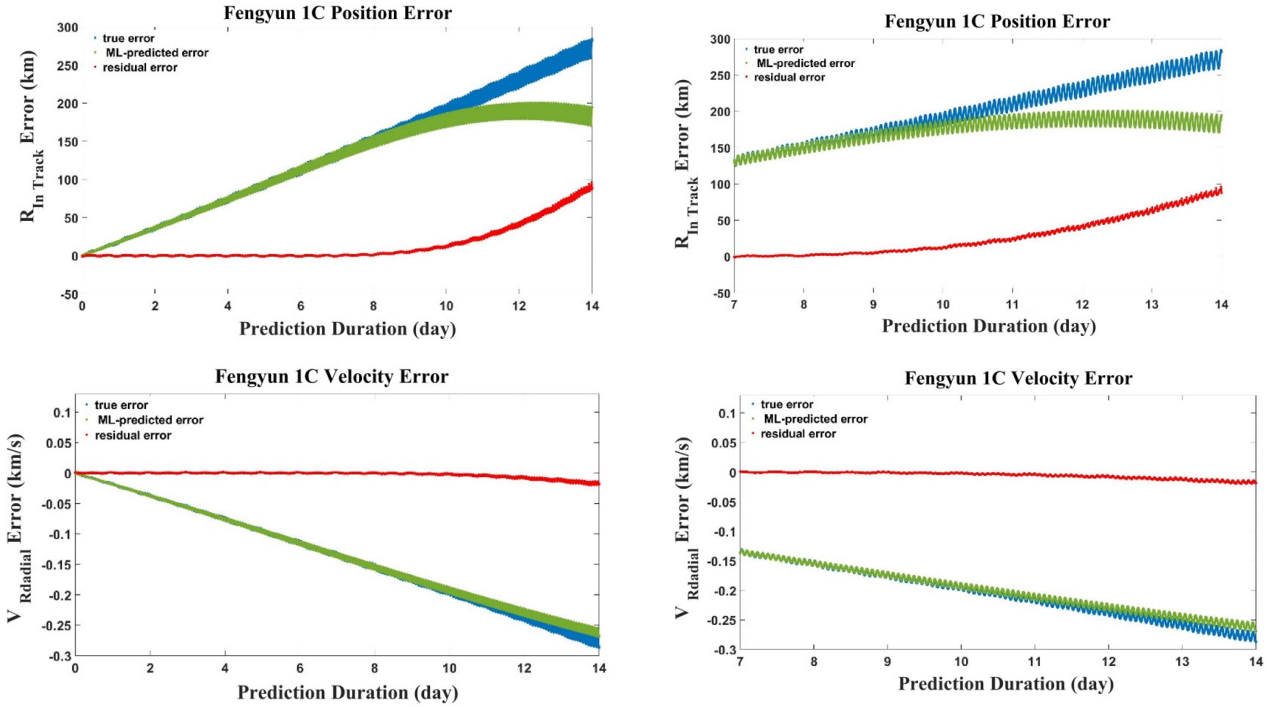

FIGURE 18. Assessment of PCA-SVM regression performance on Fengyun 1C with 5 arcseconds optical sensor error.

model demonstrates satisfactory performance for an extended three-day prediction duration. However, beyond this point, the predictions start to diverge gradually.

Furthermore, it's worth noting that in all simulations under various conditions, the results show that the MAE consistently yields lower values across all cases presented in the tables. While MAE may indicate better performance in terms of accuracy compared to other metrics such as MSE, RMSE, or R-squared, it is essential to consider the specific objectives and constraints of the analysis when interpreting these results. In some applications, lower values of MAE may indicate better accuracy and may be more desirable if

they meet the requirements of the intended use case. For example, if the primary concern is the absolute deviation between predicted and observed values, MAE may provide a straightforward measure of accuracy that aligns with the application's goals. However, it is also crucial to consider the relative strengths and weaknesses of each metric in different contexts. Metrics such as MSE and RMSE emphasize the squared differences between predicted and observed values, which may penalize large errors more heavily compared to MAE. On the other hand, R2 score provides a measure of the proportion of variance explained by the model, offering insights into the goodness of fit. A comprehensive evaluation should consider multiple metrics in conjunction to provide a holistic assessment of the model's performance. Depending on the specific objectives and constraints of the analysis, one metric may be more suitable than others.

VI. CONCLUSION

This study investigates the crucial problem of LEO orbital debris and proposes an innovative solution to enhance space debris tracking and orbit prediction accuracy. The CAM strategy, utilized as the primary countermeasure for mitigating the threat posed by LEO space debris, depends significantly on precise knowledge of debris coordinates and accurate trajectory predictions, both of which present substantial challenges in the dynamic LEO environment. Traditional ground-based observation methods encounter challenges due to atmospheric interference and limited FOV, impacting their effectiveness in tracking fast-moving debris in the dynamic LEO environment. Additionally, conventional orbit prediction models' uncertainties, stemming from unknown coefficients of perturbation forces and other debris characteristics, lead to prediction errors.

To overcome these limitations, the research proposes an innovative solution using an in-orbit optical space surveillance system. This system comprises a network of distributed optical sensors deployed on multiple spacecraft within the ATH constellation, specifically designed to monitor the densely populated altitude band in LEO. Furthermore, a novel orbit prediction model is introduced, leveraging a supervised ML approach, specifically SVM regression. The model's performance is optimized by incorporating PCA, an unsupervised ML approach, to reduce the dimensionality of the dataset's feature space.

The proposed ML scheme aims to enhance the accuracy of space debris orbit prediction by learning from historical data in a simulated environment. Simulation results under various conditions demonstrate the scheme's successful complementation of ground-based equipment and dynamic models for debris tracking, significantly improving orbit prediction accuracy.

REFERENCES

[1] D. Cerutti-Maori, J. Osebrock, C. Carloni, M. Budoni, I. Maouloud, and J. Klare, "A novel high-precision observation mode for the tracking and imaging radar TIRA-principle and performance evaluation," in *Proc. 8th Eur. Conf. Space Debris*, 2021, pp. 1–12.

[2] A. De Vittori, R. Cipollone, P. Di Lizia, and M. Massari, "Real-time space object tracklet extraction from telescope survey images with machine learning," *Astrodynamics*, vol. 6, no. 2, pp. 205–218, Jun. 2022, doi: 10.1007/s42064-022-0134-4.

[3] (2023). *European Space Surveillance and Tracking*. [Online]. Available: https://www.eusst.eu

[4] A. Milani, G. Tommei, D. Farnocchia, A. Rossi, T. Schildknecht, and R. Jehn, "Correlation and orbit determination of space objects based on sparse optical data," *Monthly Notices Roy. Astronomical Soc.*, vol. 417, no. 3, pp. 2094–2103, Nov. 2011, doi: 10.1111/j.1365-2966.2011.19392.x.

[5] A. Milani, D. Farnocchia, L. Dimare, A. Rossi, and F. Bernardi, "Innovative observing strategy and orbit determination for low Earth orbit space debris," *Planet. Space Sci.*, vol. 62, no. 1, pp. 10–22, Mar. 2012, doi: 10.1016/j.pss.2011.11.012.

[6] M. Romano, A. Muciaccia, M. Trisolini, C. Colombo, P. Di Lizia, A. Di Cecco, and L. Salotti, "Puzzle software for the characterization of in-orbit fragmentations," in *Proc. 8th Eur. Conf. Space Debris*, 2021, pp. 1–12.

[7] G. Tommei, A. Milani, and A. Rossi, "Orbit determination of space debris: Admissible regions," *Celestial Mech. Dyn. Astron.*, vol. 97, no. 4, pp. 289–304, Apr. 2007, doi: 10.1007/s10569-007-9065-x.

[8] T. Yanagisawa, H. Kurosaki, H. Oda, and M. Tagawa, "Ground-based optical observation system for LEO objects," *Adv. Space Res.*, vol. 56, no. 3, pp. 414–420, Aug. 2015, doi: 10.1016/j.asr.2015.01.019.

[9] B. Gong, S. Wang, S. Li, and X. Li, "Review of space relative navigation based on angles-only measurements," *Astrodynamics*, vol. 7, no. 2, pp. 131–152, Jun. 2023, doi: 10.1007/s42064-022-0152-2.

[10] J. G. Walker, "Some circular orbit patterns providing continuous whole Earth coverage," *J. Brit. Interplanetary Soc.*, vol. 24, pp. 369–384, Jan. 1971.

[11] T. J. Lang, "Optimal low Earth orbit constellations for continuous global coverage," *Adv. Astronaut. Sci.*, vol. 85, no. 2, pp. 1199–1216, 1993.

[12] D. Beste, "Design of satellite constellations for optimal continuous coverage," *IEEE Trans. Aerosp. Electron. Syst.*, vols. AES-14, no. 3, pp. 466–473, May 1978, doi: 10.1109/TAES.1978.308608.

[13] J. E. Draim, "Three and four-satellite continuous coverage constellations," *J. Guid. Control. Dyn.*, vol. 8, no. 6, pp. 725–730, 1985.

[14] J. E. Draim, "A common-period four-satellite continuous global coverage constellation," *J. Guid., Control Dyn.*, vol. 10, no. 5, pp. 492–499, Sep. 1987, doi: 10.2514/3.20244.

[15] J. E. Draim, "Continuous global N-tuple coverage with (2N + 2) satellites," *J. Guid., Control Dyn.*, vol. 14, no. 1, pp. 17–23, Jan. 1991, doi: 10.2514/3.20599.

[16] L. Rider, "Design of low to medium altitude surveillance systems providing continuous multiple above-the-horizon viewing," *Opt. Eng.*, vol. 28, no. 1, pp. 1–17, Jan. 1989, doi: 10.1117/12.7976896.

[17] L. Rider, "Optimized polar orbit constellations for redundant Earth coverage," *J. Astronaut. Sci.*, vol. 33, no. 2, pp. 147–161, 1985.

[18] A. D. Biria and B. G. Marchand, "Constellation design for space-based space situational awareness applications: An analytical approach," *J. Spacecraft Rockets*, vol. 51, no. 2, pp. 545–562, Mar. 2014, doi: 10.2514/1.a32622.

[19] A. T. Takano and B. G. Marchand, "Optimal constellation design for space based situational awareness applications," *Adv. Astronaut. Sci.*, vol. 142, pp. 2139–2158, 2012.

[20] X. Lei, S. Xia, Y. Yang, X. Wang, Z. Zhang, Z. Li, and J. Sang, "Comparison of initial orbit determination methods with very-short-arc angle observations from LEO space debris," *Chin. J. Space Sci.*, vol. 42, no. 5, p. 984, 2022, doi: 10.11728/cjss2022.05.211026108.

[21] J. Qu, T. Fu, D. Chen, H. Cao, and S. Zhang, "An analytical initial orbit determination method using two observations from a bistatic radar," *Adv. Space Res.*, vol. 70, no. 7, pp. 1949–1964, Oct. 2022, doi: 10.1016/j.asr.2022.06.070.

[22] L. Cament, M. Adams, and P. Barrios, "Space debris tracking with the Poisson labeled multi-Bernoulli filter," *Sensors*, vol. 21, no. 11, p. 3684, May 2021, doi: 10.3390/s21113684.

[23] C. Levit and W. Marshall, "Improved orbit predictions using two-line elements," *Adv. Space Res.*, vol. 47, no. 7, pp. 1107–1115, Apr. 2011, doi: 10.1016/j.asr.2010.10.017.

[24] L. Chen et al., "Orbital error analysis based on historical data," in *Orbital data applications for space objects*. Singapore: Springer, 2017, ch. 3, pp. 77–105, doi: 10.1007/978-981-10-2963-9.

[25] S. T. Goh, J. W. Chia, S. T. Chin, K. S. Low, and L. S. Lim, "A pre-processed orbital parameters approach for improving cubesat orbit propagator and attitude determination," *Trans. Jpn. Soc. Aeronaut. Space Sci.*, vol. 59, no. 5, pp. 278–286, 2016, doi: 10.2322/tjsass.59.278.
[26] J. Sang, B. Li, J. Chen, P. Zhang, and J. Ning, "Analytical representations of precise orbit predictions for Earth orbiting space objects," *Adv. Space Res.*, vol. 59, no. 2, pp. 698–714, Jan. 2017, doi: 10.1016/j.asr.2016.10.031.
[27] D. Pérez and R. Bevilacqua, "Neural network based calibration of atmospheric density models," *Acta Astronautica*, vol. 110, pp. 58–76, May 2015, doi: 10.1016/j.actaastro.2014.12.018.
[28] S. Sharma, J. W. Cutler, S. Sharma, and J. W. Cutler, "Robust orbit determination and classification: A learning theoretic approach," *Interplanet. Netw. Prog. Rep.*, vols. 42–203, pp. 1–20, Jun. 2015.
[29] H. Peng and X. Bai, "Improving orbit prediction accuracy through supervised machine learning," *Adv. Space Res.*, vol. 61, no. 10, pp. 2628–2646, May 2018, doi: 10.1016/j.asr.2018.03.001.
[30] H. Peng and X. Bai, "Gaussian processes for improving orbit prediction accuracy," *Acta Astronautica*, vol. 161, pp. 44–56, Aug. 2019, doi: 10.1016/j.actaastro.2019.05.014.
[31] H. Peng and X. Bai, "Comparative evaluation of three machine learning algorithms on improving orbit prediction accuracy," *Astrodynamics*, vol. 3, no. 4, pp. 325–343, Dec. 2019, doi: 10.1007/s42064-018-0055-4.
[32] O. Jung, J. Seong, Y. Jung, and H. Bang, "Recurrent neural network model to predict re-entry trajectories of uncontrolled space objects," *Adv. Space Res.*, vol. 68, no. 6, pp. 2515–2529, Sep. 2021, doi: 10.1016/j.asr.2021.04.041.
[33] M. Zhai, Z. Huyan, Y. Hu, Y. Jiang, and H. Li, "Improvement of orbit prediction accuracy using extreme gradient boosting and principal component analysis," *Open Astron.*, vol. 31, no. 1, pp. 229–243, Jun. 2022, doi: 10.1515/astro-2022-0030.
[34] Y. Takahashi, M. Saito, N. Oshima, and K. Yamada, "Trajectory reconstruction for nanosatellite in very low Earth orbit using machine learning," *Acta Astronautica*, vol. 194, pp. 301–308, May 2022, doi: 10.1016/j.actaastro.2022.02.010.
[35] B. Li, Y. Zhang, J. Huang, and J. Sang, "Improved orbit predictions using two-line elements through error pattern mining and transferring," *Acta Astronautica*, vol. 188, pp. 405–415, Nov. 2021, doi: 10.1016/j.actaastro.2021.08.002.
[36] N. Salleh, N. F. Mohd Azmi, and S. S. Yuhaniz, "An adaptation of deep learning technique in orbit propagation model using long short-term memory," in *Proc. Int. Conf. Electr., Commun., Comput. Eng. (ICECCE)*, Jun. 2021, pp. 1–6, doi: 10.1109/ICECCE52056.2021.9514264.
[37] X. Xu, H. Wen, H. Song, and Y. Zhao, "A DT machine learning-based satellite orbit prediction for IoT applications," *IEEE Internet Things Mag.*, vol. 6, no. 2, pp. 96–100, Jun. 2023, doi: 10.1109/IOTM.001.2200271.
[38] C. Pardini and L. Anselmo, "Evaluating the impact of space activities in low Earth orbit," *Acta Astronautica*, vol. 184, pp. 11–22, Jul. 2021, doi: 10.1016/j.actaastro.2021.03.030.
[39] W. S. Adams and L. Rider, "Circular polar constellations providing continuous single or multiple coverage above a specified latitude," *J. Astronaut. Sci.*, vol. 35, no. 2, pp. 155–192, 1987.
[40] R. D. Luders, "Satellite networks for continuous zonal coverage," *ARS J.*, vol. 31, no. 2, pp. 179–184, Feb. 1961, doi: 10.2514/8.5422.
[41] L. Ansalone and F. Curti, "A genetic algorithm for initial orbit determination from a too short arc optical observation," *Adv. Space Res.*, vol. 52, no. 3, pp. 477–489, Aug. 2013, doi: 10.1016/j.asr.2013.04.004.
[42] G. Sciré, F. Santoni, and F. Piergentili, "Analysis of orbit determination for space based optical space surveillance system," *Adv. Space Res.*, vol. 56, no. 3, pp. 421–428, Aug. 2015, doi: 10.1016/j.asr.2015.02.031.
[43] Y. Wang, S. Sun, and L. Li, "Adaptively robust unscented Kalman filter for tracking a maneuvering vehicle," *J. Guid., Control, Dyn.*, vol. 37, no. 5, pp. 1696–1701, Sep. 2014, doi: 10.2514/1.g000257.
[44] K. Li, L. Chang, and B. Hu, "A variational Bayesian-based unscented Kalman filter with both adaptivity and robustness," *IEEE Sensors J.*, vol. 16, no. 18, pp. 6966–6976, Sep. 2016, doi: 10.1109/JSEN.2016.2591260.
[45] Y. Huang, Y. Zhang, Z. Wu, N. Li, and J. Chambers, "A novel adaptive Kalman filter with inaccurate process and measurement noise covariance matrices," *IEEE Trans. Autom. Control*, vol. 63, no. 2, pp. 594–601, Feb. 2018, doi: 10.1109/TAC.2017.2730480.
[46] Z. Li, Y. Wang, and W. Zheng, "Space-based optical observations on space debris via multipoint of view," *Int. J. Aerosp. Eng.*, vol. 2020, pp. 1–12, Feb. 2020, doi: 10.1155/2020/8328405.
[47] J. E. Hippelheuser and T. A. Elgohary, "New geometric approach for multi-node space-based orbit estimation," in *Proc. 2nd IAA Conf. Space Situational Awareness*, 2020, pp. 1–6.
[48] T. H. Tasif, J. E. Hippelheuser, and T. A. Elgohary, "Analytic continuation extended Kalman filter framework for perturbed orbit estimation using a network of space-based observers with angles-only measurements," *Astrodynamics*, vol. 6, no. 2, pp. 161–187, Jun. 2022, doi: 10.1007/s42064-022-0138-0.
[49] L. Felicetti and M. R. Emami, "A multi-spacecraft formation approach to space debris surveillance," *Acta Astronautica*, vol. 127, pp. 491–504, Oct. 2016, doi: 10.1016/j.actaastro.2016.05.040.
[50] B. Jia et al., "Cooperative space object tracking using space-based optical sensors via consensus-based filters," *IEEE Trans. Aerosp. Electron. Syst.*, vol. 52, no. 4, pp. 1908–1936, 2016, doi: 10.1109/TAES.2016.140506.
[51] L. Rider, "Nadir hole-fill by adjacent satellites in a single orbit," *Astronaut. Sci.*, vol. 28, no. 3, pp. 299–305, 1980.
[52] D. A. Vallado, *Fundamentals of Astrodynamics and Applications*, 3rd ed. Cham, Switzerland: Springer, 2007.
[53] J.-C. Liou and N. L. Johnson, "Characterization of the cataloged fengyun-1C fragments and their long-term effect on the LEO environment," *Adv. Space Res.*, vol. 43, no. 9, pp. 1407–1415, May 2009, doi: 10.1016/j.asr.2009.01.011.
[54] J. Nicholas, "The collision of iridium 33 and cosmos 2251: The shape of things to come," in *Proc. Int. Astron. Congr.*, 2251, pp. 1–17.
[55] J. Murray, T. Kennedy, and M. Matney. (2022). *Observations of Small Debris From the Cosmos 1408 Anti-Satellite Test Using the HUSIR and Goldstone Radars*. [Online]. Available: https://amostech.com/
[56] J. M. Picone, A. E. Hedin, D. P. Drob, and A. C. Aikin, "NRLMSISE-00 empirical model of the atmosphere: Statistical comparisons and scientific issues," *J. Geophys. Res., Space Phys.*, vol. 107, no. A12, pp. 1–12, Dec. 2002, doi: 10.1029/2002ja009430.
[57] S. P. Hughes, *General Mission Analysis Tool (GMAT)*. Washington, DC, USA: NASA, 2016.
[58] (2016). *STELA 3.1.1 User Manual. Tech. rep. Centre National D'tudes Spatiales*. [Online]. Available: http://stella-archive.aip.de/stella/doc/StellaServiceManual/build/latex/StellaServiceManual.pdf

SARA HAMIDIAN was born in Tehran, Iran, in 1984. She received the M.S. degree in electrical engineering from the Amirkabir University of Technology, Tehran, in 2011. She is currently pursuing the Ph.D. degree in aerospace engineering with the University of Tehran, Iran.

Since 2020, she has been a Teacher Assistant with the Department of Aerospace Engineering, Faculty of New Sciences and Technologies, University of Tehran. Her research interests include the development of satellite orbit estimation and prediction techniques, navigation, and machine learning. In the realm of academic achievement, she holds the top grade in her field at the university.

AMIR REZA KOSARI received the B.S. degree in aerospace engineering from the Amirkabir University of Technology, and the M.S. and Ph.D. degrees in aerospace engineering from the Sharif University of Technology, Tehran, Iran, in 2008.

Since 2014, he has been an Associate Professor with the Aerospace Engineering Department, Faculty of New Sciences and Technologies, University of Tehran, Iran. He has been the Director of the Systems Engineering Department, Aerospace and Advanced Systems Research Institute, University of Tehran, since 2014; the Head of the Aerospace Department, Faculty of New Sciences and Technologies, since 2018; and the Director of the Flight Performance of Aerospace Systems Laboratory, since 2019. His research interests include advanced control, optimal control, flight dynamics and control of the spacecraft, and guidance and navigation.

Prof. Kosari was a recipient of the first Khayyam Annual National Award for Excellence, in 2018. He achieved the first place in the fifth CanSat National Championship, Iran, in 2017; and the Silver Medal in third International CanSat Competition LEEM-UPM 2012–CanSat, Europe, in 2012.